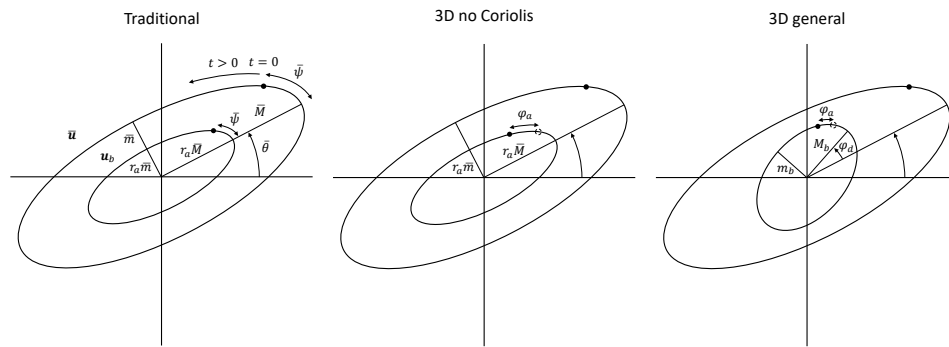


Graphical Abstract

The relationship between linearised 3D and 2DH models for tidally dominated shallow waters

Marco P. Rozendaal, Yoei M. Dijkstra, Henk M. Schuttelaars



Highlights

The relationship between linearised 3D and 2DH models for tidally dominated shallow waters

Marco P. Rozendaal, Yoei M. Dijkstra, Henk M. Schuttelaars

- In general, 3D and 2DH models produce different depth-averaged dynamics
- These differences are caused by 3D friction effects
- These are mainly caused by the near-bed velocity leading the depth-averaged velocity
- For harmonic waves, these effects are especially important for small Stokes numbers

The relationship between linearised 3D and 2DH models for tidally dominated shallow waters

Marco P. Rozendaal^{a,*}, Yoei M. Dijkstra^a, Henk M. Schuttelaars^a

^a*Delft Institute of Applied Mathematics, Delft University of Technology, Delft, The Netherlands*

Abstract

The water motion computed using 3D and 2DH models in tidally dominated shallow waters can, in some cases, differ significantly. In 2DH models, bed friction is traditionally parametrised as being proportional to the depth-averaged velocity, whereas in 3D models, bed friction depends on the near-bed velocity, which is generally not proportional to the depth-averaged velocity. Focussing on linearised models, we derive an exact friction parametrisation for 2DH models such that the same depth-averaged dynamics are described as in the corresponding 3D model. The result is a convolutional friction formulation where the instantaneous friction depends on the present and past velocities, thus modifying the traditional 2DH friction formulation that only depends the present depth-averaged velocity. In the case of harmonic (tidal) waves, this parametrisation has a clear physical interpretation and shows that the near-bed velocity should be parametrised as a rotated, deformed and phase shifted variant of the depth-averaged velocity rather than being proportional to the depth-averaged velocity. We demonstrate that in certain regions of the parameter space, it may be impossible to calibrate a 2DH model that uses a traditional friction law to reproduce the water levels from a 3D model, showing that the 3D friction formulation can be crucial to capture the 3D dynamics within a depth-averaged model.

Keywords:

Idealised model, 3D model, 2DH model, 3D friction formulation

*Corresponding author

Email address: M.P.Rozendaal@tudelft.nl (Marco P. Rozendaal)

1. Introduction

Estuaries and shelf seas are important coastal features that can be found all over the world. The water motion in these shallow regions is not only important to understand for safety reasons, but is also crucial for the transport of constituents, such as salt, sediments and nutrients (Wong, 1994; Li and O'Donnell, 1997; Stacey et al., 2001). The vertical structure of the water motion plays an essential role in mixing and redistributing these substances throughout the water column (Fischer, 1972; Dyer, 1974). As a consequence, the water motion is inherently three dimensional, even in these shallow regions. Since tides are an important driver of the water motion, it is important to understand their three-dimensional structure. However, our current understanding of tidal dynamics is largely based upon linearised depth-averaged two-dimensional horizontal (2DH) models (Taylor, 1922; Friedrichs, 2010; Roos et al., 2011). These models have, for example, been used to explain quarter wavelength resonance (Defant, 1961), cross-channel half-wave resonance (Huthnance, 1980), radiation damping (Garrett, 1975) and amphidromic points (Taylor, 1922). In this approach, it is implicitly assumed that a depth-averaged model is able to capture the three-dimensional water motion sufficiently well in order to describe, for example, the water levels, transport of water and derived properties, such as resonance lengths and characteristics.

The key difference between 3D and 2DH models is that a 3D model resolves the vertical structure of the velocity profile whereas a 2DH model only describes the behaviour of the depth-averaged velocity. By only resolving the depth-averaged velocity, it follows that processes that depend on a local velocity, e.g., at the free surface or bed, must be parametrised in terms of the depth-averaged velocity. The bed shear stress τ_b is often a dominant dissipation mechanism in shallow waters, so an accurate description of this stress is crucial. In 3D models, the bed shear stress is typically parametrised in terms of the near-bed velocity \mathbf{u}_b . This leads to the classical quadratic friction law (see, e.g., Vreugdenhil, 1994) and the associated linearised friction law (see, e.g., Hulscher, 1996):

$$\frac{\tau_b}{\rho} = s_f \mathbf{u}_b. \quad (1)$$

Here, ρ is the density of water and s_f a bed roughness coefficient. In depth-averaged models, the bed shear stress must be parametrised in terms of the depth-averaged velocity $\bar{\mathbf{u}}$. When considering a linearised bed shear stress

this traditionally results in a relation of the form (see, e.g., Schramkowski et al., 2002):

$$\frac{\tau_b}{\rho} = r\overline{\mathbf{u}}, \quad (2)$$

with r the bottom friction coefficient.

There is ample evidence in the literature that there are differences between the water motion computed using 3D and 2DH models (see, e.g., Marinone, 2000; Glock et al., 2019). Three reasons for these differences have been suggested. Firstly, Mofjeld (1980) has compared the wavenumbers corresponding to the 3D and 2DH solutions for these friction formulations and found subtle differences. One of the reasons he mentions for this discrepancy is that the parametrisation of the bed shear stress in terms of the depth-averaged velocity assumes that it acts in the same direction as the depth-averaged velocity. However, the rotation of earth causes veering in the bottom boundary layer such that the direction of the bed shear stress may not point in the same direction as the depth-averaged velocity. An example of this veering was provided by Soulsby (1981), showing observations where the bottom current was directed 48° clockwise of the surface current. Secondly, a theoretical analysis was performed by Vreugdenhil (1994) to check the validity of the parametrisation of the velocity near the bed in terms of the depth-averaged velocity in a highly simplified 2DV model for which simple analytic solutions exist. He found that there is a phase difference between the velocity near the bed and the depth-averaged velocity for harmonic signals. This phase difference was also observed earlier by, e.g., Prandle (1982); Soulsby (1983). Thirdly, Zielke (1966) considered the friction formulation for transient pipe flow. He derived a frequency dependent friction formulation to exactly parametrise the wall shear stress in a cross-sectionally-averaged model and showed that this formulation better matched the observed resonance behaviour than a friction formulation that did not depend on the frequency.

In conclusion, differences between the depth-averaged results of 3D and 2DH models have been observed and three effects have been identified. However, it remains unclear how to include these three effects in a consistent manner in a 2DH model such that this model and a 3D model describe the same depth-averaged dynamics. In view of this, the main aim of this contribution is to derive a consistent parametrisation of the bed shear stress for 2DH models such that the same depth-averaged dynamics are obtained as in the related 3D model.

The structure of this paper is as follows. First the linearised three-dimensional and corresponding 2DH model are presented. For a single harmonic component, the relationship between the depth-average and depth-resolving model is derived and an interpretation using tidal ellipses is given. Then the general relationship is presented for arbitrary time signals.

2. Model formulation

2.1. The 3D hydrodynamic equations

The linearised incompressible three-dimensional Reynolds-averaged shallow water equations are often used to describe the water motion in shelf seas and estuaries (Mofjeld, 1980; Winant, 2007). In these equations, the hydrostatic balance, the Boussinesq approximation, the eddy viscosity formulation and the f -plane approximation are used and the non-linearities have been linearised or neglected using scaling arguments. Neglecting density gradients, these equations read

$$\begin{cases} \zeta_t + \left(\int_{-H}^R u \, dz \right)_x + \left(\int_{-H}^R v \, dz \right)_y = 0, \\ u_t - fv = -g\zeta_x + (A_\nu u_z)_z, \\ v_t + fu = -g\zeta_y + (A_\nu v_z)_z, \end{cases} \quad (3)$$

where, $\zeta(x, y, t)$ is the free surface, $\mathbf{u}(x, y, z, t) = (u, v)^T$ represents the horizontal velocity vector, x, y and z are the three Cartesian coordinates in a right-handed coordinate system with z pointing upwards, t is time, f the Coriolis parameter, g the acceleration of gravity, $R(x, y)$ a subtidal surface level, $-H(x, y)$ is the bed level and $A_\nu(x, y)$ is the vertical eddy viscosity. It is assumed that the eddy viscosity parameter A_ν is uniform in the vertical dimension. The subscripts x, y, z and t denote taking the partial derivative with respect to these variables. The first equation is the depth-integrated continuity equation and the last two equations describe the conservation of momentum in the two horizontal dimensions.

At the free surface, which in the linearised formulation is found at the subtidal reference level $z = R$, a no-stress boundary condition is imposed:

$$A_\nu \mathbf{u}_z = \mathbf{0}, \quad \text{at } z = R, \quad (4)$$

whereas at the bottom, the bed shear stress is imposed through the partial-slip condition (see, e.g, Eq. (1) or Schramkowski and De Swart, 2002):

$$\frac{\boldsymbol{\tau}_b}{\rho} \equiv A_\nu \mathbf{u}_z = s_f \mathbf{u}_b, \quad \text{at } z = -H. \quad (5)$$

Here, $s_f(x, y)$ is the partial-slip coefficient. For these boundary conditions to remain valid, it is assumed that the changes in the subtidal surface level and bed are gradual throughout the domain, i.e., the magnitude of their gradients is assumed to remain small.

At the lateral boundaries connected to the sea $\partial\Omega_{\text{sea}}$, the tidal amplitude A is imposed:

$$\zeta = A(x, y, t), \quad \text{at } \partial\Omega_{\text{sea}}, \quad (6)$$

and at the closed lateral walls $\partial\Omega_{\text{wall}}$, a no-transport condition is prescribed:

$$\left(\int_{-H}^R \mathbf{u} dz \right) \cdot \mathbf{n} = 0, \quad \text{at } \partial\Omega_{\text{wall}}. \quad (7)$$

2.2. The 2DH hydrodynamic equations

To obtain the 2DH hydrodynamic equations, the 3D hydrodynamic equations (3) are integrated over the depth and the no-stress and partial-slip boundary conditions (4)–(5) are used. The depth-averaged shallow water equations solving for the free surface $\zeta(x, y, t)$ and the depth-averaged velocity components $\bar{u}(x, y, t)$, $\bar{v}(x, y, t)$ read

$$\begin{cases} \zeta_t + (D\bar{u})_x + (D\bar{v})_y = 0, \\ \bar{u}_t - f\bar{v} = -g\zeta_x - \frac{1}{D}s_f u_b, \\ \bar{v}_t + f\bar{u} = -g\zeta_y - \frac{1}{D}s_f v_b. \end{cases} \quad (8)$$

Here, $D(x, y) = H(x, y) + R(x, y)$ is the local water depth and the bar $\overline{[\cdot]}$ denotes the depth-averaging operator defined as

$$\overline{[\cdot]} = \frac{1}{D} \int_{-H}^R [\cdot] dz.$$

At the boundaries connected to the sea or ocean, the tidal amplitude is imposed:

$$\zeta = A(x, y, t), \quad \text{at } \partial\Omega_{\text{sea}}, \quad (9)$$

and at the closed walls, a no-transport condition is prescribed for non-zero depths D :

$$\bar{\mathbf{u}} \cdot \mathbf{n} = 0, \quad \text{at } \partial\Omega_{\text{wall}}. \quad (10)$$

To obtain a closed system of equations, the unresolved near-bed velocity components u_b , v_b still need to be parametrised in terms of the resolved depth-averaged velocity components \bar{u} , \bar{v} . To this end, we assume there exists a linear operator \mathcal{L} such that the bed shear stress of the 3D model is exactly recreated in the 2DH model:

$$s_f \mathbf{u}_b = \mathcal{L}\{\bar{\mathbf{u}}\}.$$

Another interpretation of the linear operator \mathcal{L} is that it shows, up to a factor s_f , how to parametrise the near-bed velocity \mathbf{u}_b in terms of the depth-averaged velocity $\bar{\mathbf{u}}$.

3. The relationship between linearised 3D and 2DH models

In this section, a systematic derivation of the operator \mathcal{L} is presented such that 3D and 2DH models describe the same depth-averaged dynamics. In section 3.1, the derivation for harmonic signals is shown and in section 3.2 the result for general time signals is given. The operator \mathcal{L} is fully analytical for both cases and in the harmonic case provides a very intuitive way to interpret the results. This case is discussed in detail.

3.1. The equivalent 2DH equations for harmonic signals

For the harmonic case, we assume that the forcing consists of a single tidal constituent with angular frequency ω . Since the 2DH hydrodynamic equations are linear, it follows that all physical quantities have the same time dependency as the forcing. Thus we may expand the free surface, depth-averaged and near-bed velocity components as follows

$$\begin{bmatrix} \zeta \\ \bar{u} \\ \bar{v} \\ u_b \\ v_b \end{bmatrix} (x, y, t) = \Re \left\{ \begin{bmatrix} Z \\ \bar{U} \\ \bar{V} \\ U_b \\ V_b \end{bmatrix} (x, y; \omega) \exp(i\omega t) \right\}. \quad (11)$$

Here, ‘ $;\omega$ ’ denotes that ω is treated as a parameter rather than a variable.

Substituting these expansions into the 2DH equations (8) results in

$$\begin{cases} i\omega Z + (D\bar{U})_x + (D\bar{V})_y = 0, \\ i\omega\bar{U} - f\bar{V} = -gZ_x - \frac{1}{D}s_f U_b, \\ i\omega\bar{V} + f\bar{U} = -gZ_y - \frac{1}{D}s_f V_b. \end{cases} \quad (12)$$

A depth-averaged model cannot explicitly resolve the bed shear stress $s_f \mathbf{U}_b$, as it only resolves the depth-averaged velocity $\bar{\mathbf{U}}$. To determine the relationship between \mathbf{U}_b and $\bar{\mathbf{U}}$, the associated 3D model (3) with harmonic forcing is used. Winant (2007) and Kumar et al. (2016) provide analytical solutions for the vertical structure of these 3D hydrodynamic equations. This allows for an exact parametrisation of the near-bed velocity in terms of the depth-averaged velocity. The resulting exact bed shear stress parametrisation in the frequency domain reads

$$s_f \mathbf{U}_b(x, y; \omega) = \mathbf{R}^{3D}(x, y; \omega) \bar{\mathbf{U}}(x, y; \omega).$$

The entries of the complex-valued 3D friction matrix can be expressed as

$$\mathbf{R}^{3D}(x, y; \omega) = s_f \begin{bmatrix} r_1 e^{i\varphi_1} & -r_2 e^{i\varphi_2} \\ r_2 e^{i\varphi_2} & r_1 e^{i\varphi_1} \end{bmatrix}.$$

Explicit analytical expressions of amplitudes $r_{1,2}$ and phases $\varphi_{1,2}$ are derived in Appendix A, where it is shown that these parameters depend in a complex (but known) way on five nondimensional numbers:

$$\mathcal{A}(x, y) = \frac{A_\nu}{s_f D}, \quad \text{Stk}_\pm(x, y; \omega) = \frac{1}{D} \sqrt{\frac{A_\nu}{|\omega \pm f|}}, \quad \mathcal{P}_\pm = \text{sign}(\omega \pm f). \quad (13)$$

The first non-dimensional parameter \mathcal{A} is the ratio between the vertical eddy viscosity A_ν and the product of the partial-slip parameter s_f and the depth D . This non-dimensional parameter may be derived from the partial-slip boundary condition. The second and third non-dimensional parameters Stk_\pm are modifications of the classical Stokes number Stk with ω replaced by $\omega \pm f$ yielding the Stokes plus Stk_+ and the Stokes min Stk_- numbers, respectively, apart from a factor $\sqrt{2}$ (Souza, 2013). The fourth and fifth nondimensional

numbers \mathcal{P}_\pm only depend on the sign of the frequency scale $\omega \pm f$ and are discretely valued. They can take the values -1, 0 and 1.

To interpret the 3D friction formulation, we transform the 2DH equations back to the time domain. This yields the equivalent 2DH equations for harmonic signals:

$$\begin{cases} \zeta_t + (D\bar{u})_x + (D\bar{v})_y = 0, \\ \bar{u}_t - f\bar{v} = -g\zeta_x - \frac{1}{D}s_f[r_1\bar{u}(t+t_1) - r_2\bar{v}(t+t_2)], \\ \bar{v}_t + f\bar{u} = -g\zeta_y - \frac{1}{D}s_f[r_1\bar{v}(t+t_1) + r_2\bar{u}(t+t_2)], \end{cases}$$

with the boundary conditions given by equations (9) and (10) and the time shift t_i for $i = 1, 2$ given by

$$t_i = \frac{\varphi_i}{\omega}.$$

Thus for harmonic signals, the linear operator \mathcal{L} is given by

$$\mathcal{L}\{\bar{\mathbf{u}}\} = s_f \begin{bmatrix} r_1\bar{u}(t+t_1) - r_2\bar{v}(t+t_2) \\ r_1\bar{v}(t+t_1) + r_2\bar{u}(t+t_2) \end{bmatrix}. \quad (14)$$

No additional assumptions have been made during the derivation of the linear operator \mathcal{L} for harmonic signals. This means that this parametrisation of the bed shear stress for 2DH models is exact; the depth-averaged and depth-resolving model describe the exact same water levels and depth-averaged velocities. This is further elaborated upon in Section 4.3.

3.1.1. Interpretation of the 3D friction formulation using the tidal ellipse

To illustrate the differences between the traditional and the 3D friction formulation for 2DH models, we introduce the linear operator $\mathcal{L}_{\text{traditional}}$ that corresponds to the traditional friction formulation, see equation (2):

$$\mathcal{L}_{\text{traditional}}\{\bar{\mathbf{u}}\} = s_f \begin{bmatrix} r_a\bar{u}(t) \\ r_a\bar{v}(t) \end{bmatrix}. \quad (15)$$

Here, we have factored the 2DH bottom friction coefficient as $r = s_f r_a$ with r_a a non-dimensional scaling parameter, to facilitate the comparison with the 3D friction formulation.

Comparing \mathcal{L} with $\mathcal{L}_{\text{traditional}}$ shows that each component of the 3D friction formulation depends, in general, on both depth-averaged velocity components that are both scaled and time (or phase) shifted with respect to the

Table 1: Definition of the near-bed tidal ellipse parameters M_b , m_b , θ_b , ψ_b and ε_b under the traditional and 3D friction formulation. The parameters \overline{M} , \overline{m} , $\overline{\theta}$, $\overline{\psi}$ and $\overline{\varepsilon}$ are the tidal ellipse parameters of the depth-averaged velocity and the parameters r_a , r_r , φ_a and φ_d follow from the (3D) friction formulation.

	M_b	m_b	θ_b	ψ_b	ε_b
Traditional	$\overline{M}r_a$	$\overline{m}r_a$	$\overline{\theta}$	$\overline{\psi}$	$\overline{\varepsilon}$
3D No Coriolis	$\overline{M}r_a$	$\overline{m}r_a$	$\overline{\theta}$	$\overline{\psi} - \varphi_a$	$\overline{\varepsilon}$
3D Coriolis	$\overline{M}r_a(1 + \overline{\varepsilon}r_r)$	$\overline{M}r_a(\overline{\varepsilon} + r_r)$	$\overline{\theta} + \varphi_d$	$\overline{\psi} - \varphi_a$	$\frac{\overline{\varepsilon} + r_r}{1 + \overline{\varepsilon}r_r}$

instantaneous depth-averaged velocity. This Cartesian form of the 3D friction formulation may be understood using Jones calculus, which is typically used to describe the elliptical polarization of light (see, e.g., Chekhova and Banzer, 2021).

To give a more physically enlightening explanation, we recall that the velocity vectors trace an ellipse over the tidal cycle. Thus both the depth-averaged and near-bed velocity trace out an ellipse. Using the 3D friction formulation, we are able to relate the near-bed tidal ellipse parameters to the depth-averaged tidal ellipse parameters. Given the depth-averaged tidal ellipse parameters, this describes how the near-bed tidal ellipse changes as a consequence of the 3D friction formulation.

We describe a tidal ellipse using 5 parameters: the magnitude of the semi-major axis M , the signed magnitude of the semi-minor axis m , the orientation of the ellipse θ , the phase of the ellipse ψ and the signed ellipticity ε (see, e.g., Souza and Simpson, 1996). The depth-averaged tidal ellipse parameters are denoted with $\overline{[\cdot]}$ and the near-bed tidal ellipse parameters with $[\cdot]_b$. The near-bed tidal ellipse parameters can be expressed in terms of the depth-averaged tidal ellipse parameters and 4 dimensionless variables: the average amplitude r_a , amplitude ratio r_r , average phase φ_a and phase deviation φ_d . These 4 dimensionless parameters follow from the (3D) friction formulation, see Table 1 and Appendix B for a derivation. In case the Coriolis parameter vanishes, the amplitude ratio r_r and phase deviation φ_d vanish.

In Fig. 1, the relationship between the depth-averaged velocity and the near-bed velocity is depicted for the traditional friction formulation (left panel), 3D no Coriolis formulation (middle panel) and the full 3D friction formulation (right panel). Below, these cases are discussed:

- The traditional formulation implicitly assumes that the near-bed veloc-

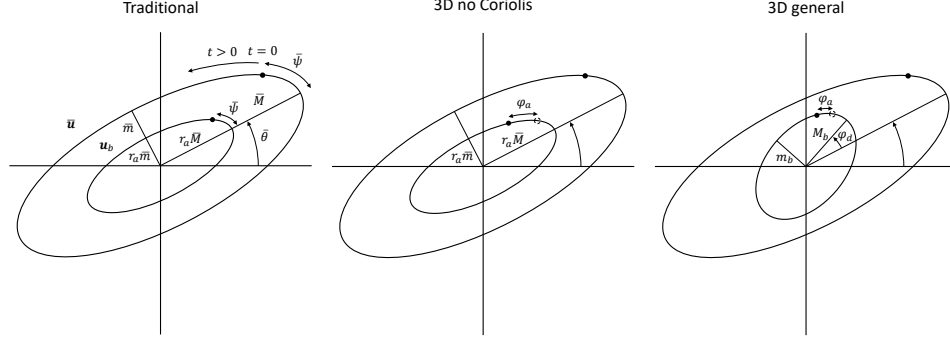


Figure 1: Graphical representation of the relationship between the depth-averaged velocity \bar{u} and the near-bed velocity u_b for the traditional, 3D no Coriolis and 3D friction formulation.

ity points in the same direction as the depth-averaged velocity. Using the scaling factor r_a , only the magnitude of the near-bed velocity can be altered. The result is that the near-bed tidal ellipse is a scaled version of the depth-averaged tidal ellipse.

- The 3D friction formulation in absence of the Coriolis force shows that the near-bed velocity still follows a scaled version of the depth-averaged ellipse, but the near-bed velocity does not necessarily point in the same direction as the depth-averaged velocity due to the possible existence of the phase shift φ_a , which is generally positive. This phase shift causes the near-bed velocity to lead the depth-averaged velocity. This phase lead can be explained as follows. The near-bed velocity is smaller than the velocity higher in the water column due to bottom friction. The water level gradient generates a depth-uniform pressure gradient. The pressure gradient acts on all fluid layers equally and produces a velocity pointing in the same direction as this gradient more rapidly in the slower-moving layers near the bed than in the layers higher in the water column (Van Rijn, 2010; Batchelor, 1967, p. 355). This causes the near-bed velocity to lead the depth-averaged velocity.
- For the full 3D friction formulation, the near-bed velocity does not point in the depth-averaged direction due to a φ_d rotation of the semi-major axis of the near-bed ellipse, a φ_a phase shift of the near-bed ellipse and an alteration of the ellipticity of the near-bed tidal ellipse

ε_b due to non-zero amplitude ratio r_r (see the right panel of Fig. 1). These effects are caused by the interaction between the Coriolis force and the vertical dimension. The Coriolis force acts perpendicular to the current velocity (with the sign dependent on the hemisphere) and it causes the velocity to rotate over the vertical. A classical example for steady currents is the Ekman spiral (see, e.g, Cushman-Roisin and Beckers, 2009). To conclude, under the 3D friction formulation, the near-bed tidal ellipse is generally rotated, deformed and phase shifted with respect to the depth-averaged tidal ellipse.

The 3D friction formulation depends in a complex way on the 5 nondimensional parameters given by equation (13). One of the parameters on which the nondimensional parameters depend is the tidal angular frequency ω . This implies that within a 2DH model, each resolved frequency component experiences a different effective friction parameter, whereas using the traditional friction formulation typically only one friction parameter r is used for all frequencies, see Appendix G for details. This somewhat counterintuitive result may be explained by considering that for each frequency ω , a different vertical profile is established in the 3D model. The differences in the vertical profile result in differences in the ratio between the depth-averaged and near-bed velocities.

While the above assumed one harmonic constituent, the derivation follows analogously when resolving multiple harmonic components. For each harmonic, the same formulation is found but with ω replaced by the considered frequency, see Appendix G for details.

3.2. The equivalent 2DH equations for general signals

The friction formulation can be generalised to arbitrary (i.e, non-harmonic) time signals using the Fourier transform. The derivation is presented in Appendix E. The resulting equivalent 2DH hydrodynamic equations in the time domain read

$$\begin{cases} \zeta_t + (D\bar{u})_x + (D\bar{v})_y = 0, \\ \bar{u}_t - f\bar{v} = -g\zeta_x - \frac{1}{D}s_f[\bar{u}(t) - (h_1 * \bar{u})(t) - (h_2 * \bar{v})(t)], \\ \bar{v}_t + f\bar{u} = -g\zeta_y - \frac{1}{D}s_f[\bar{v}(t) - (h_1 * \bar{v})(t) + (h_2 * \bar{u})(t)], \end{cases} \quad (16)$$

with the boundary conditions given by equations (9) and (10). Here, the symbol $*$ denotes the convolution operator and $h_1(x, y, t)$, $h_2(x, y, t)$ are

known frictional convolution kernels. The convolutional 3D friction formulation prescribes an instantaneous friction value based on the instantaneous depth-averaged velocity and its history (weighted according to the convolution kernels) instead of time shifted velocities as was the case for a single harmonic component. For a derivation of the friction kernels and explicit analytical expressions, we refer to Appendix E.

Thus for general time signals, the linear operator \mathcal{L} , representing the bed shear stress, is given by

$$\mathcal{L}\{\bar{\mathbf{u}}\} = s_f \left[\frac{\bar{u}(t) - (h_1 * \bar{u})(t) - (h_2 * \bar{v})(t)}{\bar{v}(t) - (h_1 * \bar{v})(t) + (h_2 * \bar{u})(t)} \right].$$

The first term in the convolutional 3D friction formulation is the same as the traditional friction formulation, showing that as a first estimate for the near-bed velocity, the depth-averaged value is recovered. However, since each frequency responds differently to the depth-averaging, history dependent correction terms are required to fully capture the 3D effect within a 2DH model.

4. Results

In this section, an interpretation of the 3D friction formulation is presented and the implications of this friction formulation are investigated.

4.1. Sensitivity of the tidal ellipse parameters of the 3D friction formulation - No Coriolis

We first concentrate on the harmonic case with no Coriolis force: $f = 0$. In this case the parameters describing the tidal ellipse for the 3D friction formulation (14) simplify (see Appendix A for analytic expressions). Since $\omega > 0$, it follows that $\mathcal{P}_{\pm} = 1$. Furthermore, since $f = 0$, the Stokes numbers Stk_+ , Stk_- reduce to the classical Stokes number Stk . As a result the average amplitude r_a and average phase φ_a only depend on the nondimensional parameters \mathcal{A} and Stk , and the amplitude ratio r_r and phase deviation φ_d vanish. The parameters r_a and φ_a may be interpreted as the scaling and phase shift between the near-bed velocity \mathbf{u}_b and the depth-averaged velocity $\bar{\mathbf{u}}$, respectively, as illustrated the middle panel of Fig. 1.

In Fig. 2, contour plots of the average amplitude r_a and average phase φ_a are shown as functions of the nondimensional parameters \mathcal{A} and Stk . The

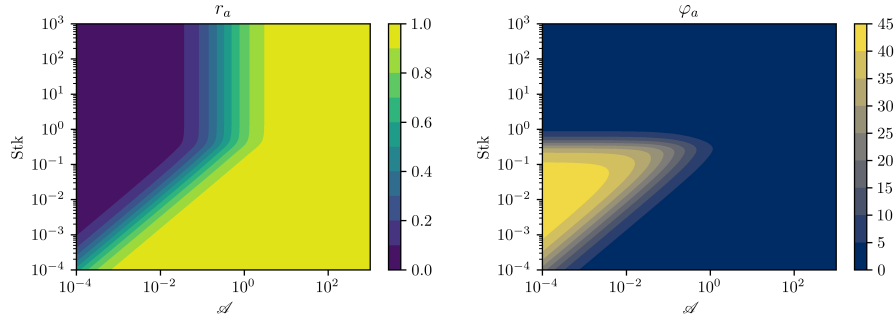


Figure 2: Contour plots of the nondimensional average amplitude r_a and average phase φ_a (in degrees) as functions of the nondimensional parameters \mathcal{A} and Stk for $\omega > 0$.

nondimensional amplitude r_a (left panel) ranges from 0 to 1. At approximately $\text{Stk} = 1$, where the frictional depth is comparable in magnitude to the local depth, the contour lines saturate and larger values of Stk do not significantly influence the value of the amplitude any more. On the other hand in the region $\text{Stk} < 1$, both parameters influence the amplitude. The amplitude is approximately constant along the diagonal line segments where Stk is proportional to \mathcal{A} . The phase shift φ_a (right panel) ranges from 0 to 45° (i.e., no phase shift for $\varphi_a = 0$ to a time advancement of $1/8$ of the wave period for $\varphi_a = 45^\circ$). For large Stokes numbers $\text{Stk} > 1$, the phase shift is very small. For smaller Stokes numbers, $\text{Stk} < 1$, a region appears where the phase shift becomes significant for small \mathcal{A} . For larger values of \mathcal{A} , the phase shift decreases to zero again. The sloped contour lines approximately occur when Stk is proportional to \mathcal{A} .

To understand these results physically, we consider two (limit) cases for the Stokes number. We consider very large Stokes numbers ($\text{Stk} \gg 1$), where the frictional depth occupies the whole water column, and very small Stokes numbers ($\text{Stk} \ll 1$), where the frictional depth occupies only a small part of the water column near the bed.

- For large Stokes numbers ($\text{Stk} \gg 1$), the nondimensional parameter \mathcal{A} fully determines the behaviour of the average amplitude r_a (left panel of Fig. 2). For small $\mathcal{A} \ll 1$, the no-slip boundary condition dominates, resulting in a near-zero velocity at the bed. As a consequence, the average amplitude r_a is approximately zero as well, as it may be interpreted as the scaling between the near-bed and depth-averaged

velocity. Conversely, for large $\mathcal{A} \gg 1$, the free-slip boundary condition is dominant, so the near-bed velocity is approximately equal to the free stream velocity. This causes the velocity profile to be approximately vertically uniform and the average amplitude r_a to be close to unity. In between these two limits, a smooth transition is found where the full partial-slip condition must be taken into account. Furthermore since the frictional depth occupies the whole water column ($\text{Stk} \gg 1$), the phase difference between the near-bed velocity and the depth-averaged velocity remains minor (right panel).

- For small Stokes numbers ($\text{Stk} \ll 1$), the effect of the bottom boundary condition is confined to a small region near the bed, a boundary layer. The thickness of this boundary layer scales with the Stokes number Stk . Rescaling the partial slip condition by the length scale of the boundary layer $\tilde{z} = (z + 1)/\text{Stk}$ yields (see Appendix C)

$$\frac{\mathcal{A}}{\text{Stk}} \mathbf{u}_{\tilde{z}} = \mathbf{u}_b.$$

Rather than comparing the magnitude of \mathcal{A} to unity as we did for large Stk , we instead compare the magnitude of \mathcal{A} to the magnitude of Stk .

Focussing on the average amplitude r_a . This means that for $\mathcal{A} \ll \text{Stk}$, the no-slip boundary condition dominates, resulting in the slanted dark blue region for r_a (left panel of Fig. 2). Conversely, for $\mathcal{A} \gg \text{Stk}$, the free-slip boundary condition dominates, yielding the slanted yellow region for r_a . For intermediate values $\mathcal{A} \approx \text{Stk}$, a transition region is found.

Regarding the average phase φ_a . For $\mathcal{A} \gg \text{Stk}$, the free-slip boundary condition dominates causing a uniform velocity profile over the whole depth and the disappearance of the boundary layer. Hence, there is almost no phase shift in this case, as depicted with the slanted dark blue region in the right panel of Fig. 2. For $\mathcal{A} \ll \text{Stk}$, a real boundary layer is formed where the velocity rapidly decreases from the free stream velocity at the top of the boundary layer to the much smaller velocity near the bed. The dynamics in the boundary layer are such that the velocity across the boundary layer attains at most a phase shift of 45° (see, e.g., Batchelor, 1967, p. 355). This is shown with the slanted yellowish region on the right panel of Fig. 2.

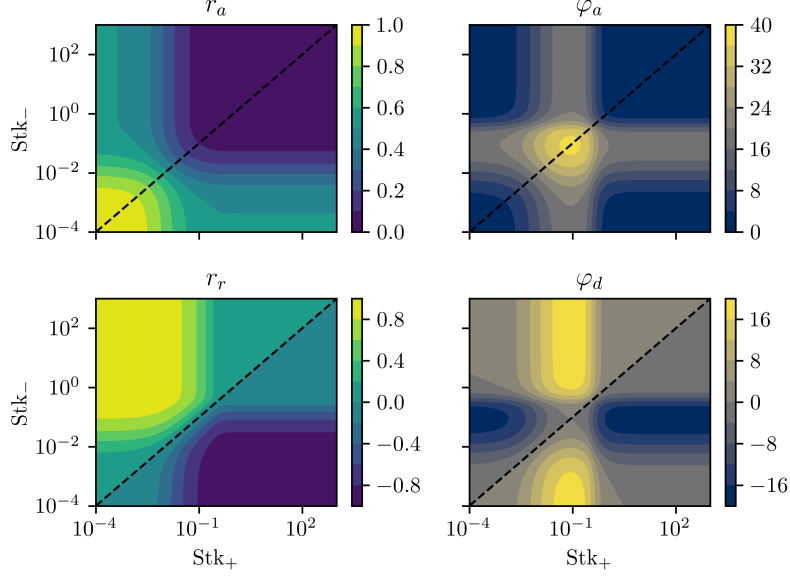


Figure 3: Contour plots of the nondimensional amplitudes r_a , r_r and phases φ_a , φ_d (in degrees) as functions of the nondimensional parameters Stk_+ and Stk_- for the nondimensional parameters $\mathcal{A} = 10^{-2}$ and $\mathcal{P}_\pm = 1$.

Using a boundary layer analysis for small Stokes numbers ($\text{Stk} \ll 1$), it can be shown that the average phase shift φ_a is indeed entirely due to the phase shift attained in the boundary layer, see Appendix C, and can be expressed as

$$\varphi_a = \arctan \left(\frac{1}{1 + \sqrt{2}\mathcal{A}/\text{Stk}} \right). \quad (17)$$

4.2. Sensitivity of the tidal ellipse parameters of the 3D friction formulation - Including Coriolis

We consider the sensitivity of the tidal ellipse parameters of the 3D friction formulation under the Coriolis force, i.e, $f \neq 0$. We assume that $|f| < \omega$ such that $\mathcal{P}_\pm = 1$.

In Fig. 3, the average amplitude r_a , amplitude ratio r_r , average phase φ_a and phase deviation φ_d are shown as functions of the nondimensional parameters Stk_+ and Stk_- for $\mathcal{A} = 10^{-2}$. The dashed diagonal lines, where $\text{Stk}_- = \text{Stk}_+ = \text{Stk}$, correspond to the no-Coriolis case. Along these diagonal lines, the average amplitude r_a and average phase φ_a correspond to the

vertical lines of the no-Coriolis case depicted in Fig. 2 with $\mathcal{A} = 10^{-2}$.

The top left panel of Fig. 3 shows the average amplitude r_a , which is largest for small Stk_\pm . When increasing either Stk_+ or Stk_- , the amplitude seems to eventually plateau to a constant value. However, if we increase both Stk_\pm the amplitude r_a goes to zero. The top right panel of Fig. 3, displays the phase shift φ_a . For $\mathcal{A} = 10^{-2}$, it attains a maximum near $\text{Stk}_\pm = 10^{-1}$. Increasing or decreasing either Stk_+ or Stk_- decreases this value until again a plateau reached. Changing both Stk_\pm , the phase shift φ_a may go to zero again. The lower left panel of Fig. 3 displays the amplitude ratio r_r . Along the diagonal line r_r vanishes and in the small Stk_+ large Stk_- regime (upper left corner), the parameter attains a maximum, conversely in the large Stk_+ small Stk_- regime (lower right corner) it attains a minimum. The lower right panel of Fig. 3 shows the phase deviation φ_d . Along the diagonal φ_d vanishes and along the lines of constant $\text{Stk}_\pm = 10^{-1}$, it attains its maximum and minimum values.

The phase shift φ_a is generally positively valued, whereas φ_d can be both positive or negative, indicating that the angle the semi-major axis of the near-bed tidal ellipse makes with the semi-major axis of the depth-averaged tidal ellipse can be both to the left and to the right depending on the sign of φ_d .

The ellipticity of the near-bed tidal ellipse can be recovered by considering the value of r_r and the ellipticity of the depth-averaged tidal ellipse $\bar{\varepsilon}$. For $r_r = 1$, the near-bed tidal ellipse becomes an anticlockwise rotating circle since $\varepsilon_b = 1$, whereas for $r_r = -1$, a clockwise rotating circle is found. If the depth-averaged velocity describes a line $\bar{\varepsilon} = 0$, then the ellipticity of the near-bed tidal ellipse is equal to $\varepsilon_b = r_r$. The near-bed tidal ellipse describes a line for $\varepsilon_b = 0$ which implies that $r_r = -\bar{\varepsilon}$.

4.3. Experiment 1: A narrow estuary

To illustrate the effect of the new 3D friction formulation, a simple test case is considered: a narrow rectangular estuary with uniform along- and across-channel parameters without the Coriolis force. The estuary is forced at the seaward side with a spatially uniform M_2 tidal constituent and the lateral and landward sides are closed. The parameter values used can be found in Table 2. The water motion within this estuary is computed using four different models: a 3D model, a 2DH model without friction, a 2DH model where the traditional friction parameter r_a is chosen such that the best possible fit with the 3D model is achieved and a 2DH model where the 3D

Table 2: The parameters used in the narrow estuary experiment.

Parameters			
Geometry	L	Length of estuary	85 km
	B	Width of estuary	1 km
	D	Depth of estuary	10 m
Earth	g	Acceleration due to gravity	9.81 m s^{-2}
	ω	M_2 angular frequency	$1.4 \times 10^{-4} \text{ s}^{-1}$
	f	Coriolis parameter	0 s^{-1}
Model	A_ν	Vertical eddy viscosity parameter	$1 \times 10^{-3} \text{ m}^2 \text{ s}^{-1}$
	s_f	Partial slip parameter	$3 \times 10^{-3} \text{ m s}^{-1}$
Forcing	A_{M_2}	M_2 amplitude at $x = 0$	1 m
	ϕ_{M_2}	M_2 phase at $x = 0$	0 deg

Table 3: The friction parameters used for the 2DH model in the narrow estuary experiment. For the traditional friction formulation, r_a is determined such that the best fit with the 3D model is achieved and for the 3D friction formulation, (r_a, φ_a) are computed directly using the 3D parameters.

	Traditional 2DH formulation (Fitted)	3D friction formulation (Calculated)
r_a	0.133	0.131
φ_a (deg)	0	28

friction parameters (r_a, φ_a) are computed using the 3D friction formulation, see Table 3.

In Fig. 4, the amplitude and phase of the water level of the M_2 tidal constituent are shown along the length of the estuary. The water motion computed using the 3D model (blue), 2DH best fit (green) and 2DH 3D friction (red) have a progressive nature near the mouth and transition into a standing wave near the landward end, whereas the water motion computed using the 2DH frictionless model (orange) is a pure standing wave. This figure shows that the results obtained using the 3D model and the 2DH model using the 3D friction formulation are identical.

Comparing the 2DH best fit with the 3D model shows a difference in amplitude of approximately 0.6 m at the landward end and a difference in phase of approximately 1° . Next, we compare the 2DH frictionless model with the

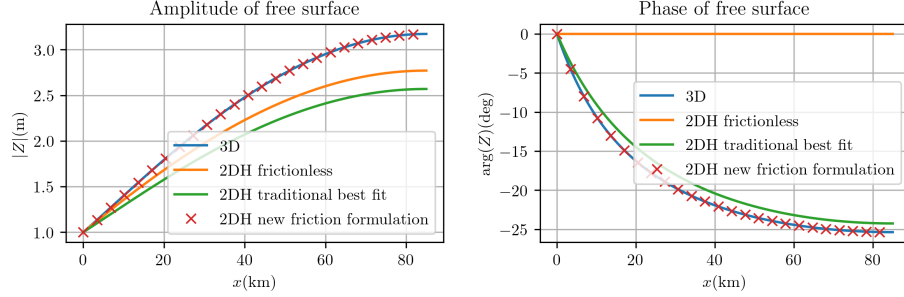


Figure 4: Amplitude and phase of the water level of the M_2 tidal constituent as function of the distance from the estuarine mouth computed using four different models.

3D model. The phase of the frictionless model does not resemble the phase of the 3D model, but more strikingly, the amplitude is approximately 0.4 m lower than in the frictional 3D model. Under the traditional 2DH friction formulation, increasing the friction always lowers the response of the estuary. However, under the 3D friction formulation, increasing the friction may lead to larger responses than the frictionless model. This suggests that a 2DH model using the traditional friction formulation is never able to reproduce the amplitudes obtained using the 3D formulation, irrespective of how one tries to calibrate the friction parameter. The mechanism responsible for this counter-intuitive result is discussed below and in Section 4.4.1.

4.4. Amplification plane

The phase shift φ_a plays an important role in the estuarine dynamics and will be investigated in more detail in this section. The effect of the phase shift φ_a on the amplitude in the estuary is studied in the absence of the Coriolis force. To this end, we consider the amplification a , which is defined as the ratio of the amplitude at the landward side and the forcing amplitude at the seaward side. For frictionally dominated systems, the amplification a tends to zero, whereas for systems close to resonance, the amplification a tends to infinity.

As a first step the amplification under the traditional friction formulation is considered. In the left panel of Fig. 5, classical amplification curves are shown as function of the nondimensional estuarine length L/λ_q , where L is the estuarine length and λ_q is the quarter wavelength of the frictionless tidal wave. For frictionless estuaries, pure resonance occurs when the estuarine length L is an odd multiple of the quarter tidal wavelength λ_q (see, e.g.,

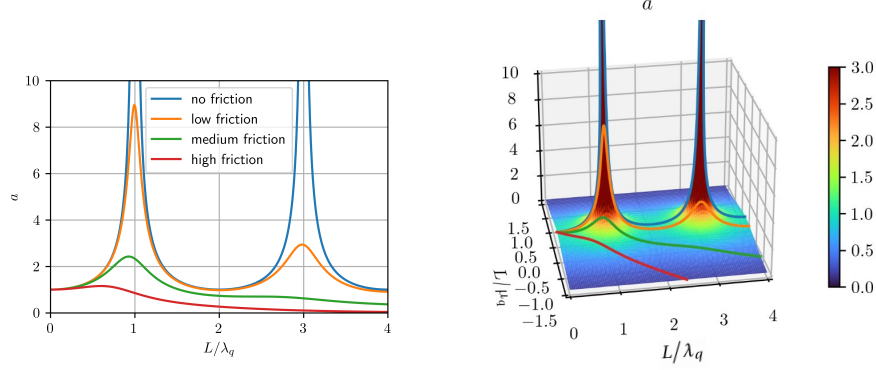


Figure 5: Left, classical amplification curves as function of the nondimensional length of the estuary for no, low, medium and high friction values. These values are merely used to indicate the effect of increasing friction on the amplification. Right, the amplification plane as function of the nondimensional estuarine length with respect to the quarter wavelength and the quarter decay length scale. The classical amplification curves are also plotted in the amplification plane.

Friedrichs, 2010; Roos et al., 2011). For frictional systems, the amplification close to the odd multiples attains a maximum and this maximum decreases as the nondimensional estuarine length increases.

The right panel of Fig. 5 shows the amplification plane where the x -axis represents the nondimensional estuarine length L/λ_q and the y -axis represents the nondimensional estuarine length L/μ_q , where μ_q is the quarter amplification length of the frictional tidal wave, which is defined as the length where the amplitude of the tidal free wave has increased by a factor $\exp(\pi/2) \approx 4.81$. Negative values indicate that the free tidal wave amplitude has decreased by the same factor. This x - y plane is proportional to the complex plane of the complex wave number κ times the estuarine length L , in particular, we have the relationship $\kappa L = \pi/2 (L/\lambda_q + iL/\mu_q)$. The no, low, medium and high friction curves are plotted in the amplification plane for reference.

4.4.1. The effect of the phase shift I

We consider three cases for the friction formulation. The frictionless formulation, the traditional 2DH friction formulation and the 3D friction formulation. Given the model parameters and friction formulation, the corresponding tidal wave length and decay length scale of the tidal wave can be

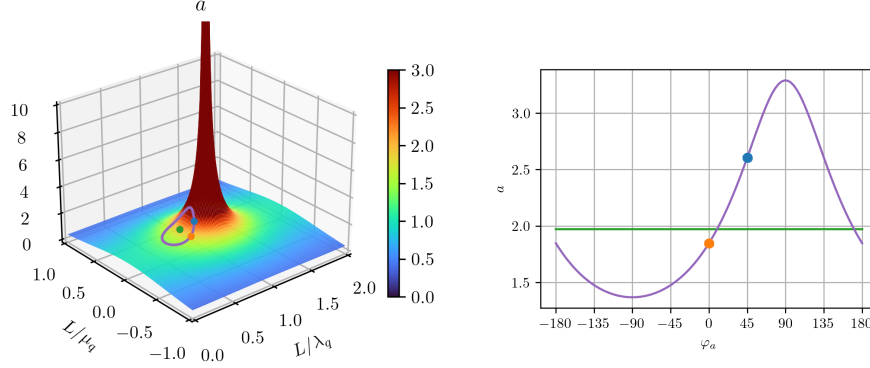


Figure 6: Left, amplification plane with a frictionless, 2DH friction and 3D friction formulation denoted by the green, orange and blue dots. The purple curve shows the effect of varying φ_a assuming it is a free parameter. Right, the amplification is plotted as a function of the phase shift φ_a , assuming it is a free parameter. The green line represents the frictionless amplification. The orange and blue dot indicate the amplification using the 2DH traditional and 3D friction formulation, respectively.

computed. Using these two numbers, a location in the amplification plane can be identified that fully characterises the amplification within the estuary. This allows for the direct comparison of the effect of different friction formulations on the estuarine amplification.

To isolate the effect of the phase shift φ_a of the 3D friction formulation, it is assumed that φ_a is a free parameter that can be varied between -180° and 180° without affecting the other parameters, whereas in reality φ_a is bounded between 0° and 45° and depends on the 3D parameters.

In the left panel of Fig. 6, the first resonant peak in the amplification plane is shown together with the amplification computed using a frictionless, 2DH friction and 3D friction formulation, denoted by respectively the green, orange and blue dot. For the 3D friction formulation the phase shift is chosen to be 45° but can also be calculated using equation (B.1). The purple curve is obtained by freely varying the phase shift parameter between -180° and 180° . By setting the phase shift to $\varphi_a = 0^\circ$, the original 2DH formulation is recovered. By increasing the phase shift to 45° , the maximal allowable phase shift under the 3D friction formulation is reached.

In the right panel of Fig. 6, the amplification along the purple curve in the amplification plane is shown as function of the phase shift parameter φ_a . The green line shows the amplification of the frictionless case, the orange

dot signifies the amplification with the traditional 2DH friction formulation and the blue dot the amplification under the maximal allowable phase shift under the 3D friction formulation. Under the 3D friction formulation, the phase shift is between 0° and 45° . If we increase the phase shift φ_a within this range the amplification increases. Even small values of the phase shift φ_a result in higher amplification than the frictionless case. This is in line with the plotted purple curve in the left panel of Fig. 6.

4.4.2. The effect of the phase shift II

We revisit the effect of the phase shift in the narrow estuary. The parameter values are chosen such that instead of the ratio between the estuarine length and the quarter frictionless tidal wavelength is smaller than 1, as was the case in section 4.4.1, this ratio is larger than 1. In terms of the amplification diagram this means that rather than being before the first resonance peak, a location after the first resonance peak is considered.

In the left panel of Fig. 7, the amplification plane is shown from behind the first resonance peak. The green, orange and blue dot again denote the response under the frictionless, 2DH traditional friction and the 45° phase shifted 3D friction formulation. Increasing φ_a from the traditional 2DH friction formulation leads again to larger L/λ_q . However, in this case, increasing the phase shift φ_a leads to lower responses since increasing L/λ_q means moving away from the first resonance peak.

In the right panel of Fig. 7, the amplification as function of the phase shift φ_a is shown. This is the same amplification as experienced when traversing the purple curve in the left panel of Fig. 7. The frictionless response is shown by the green line, the orange dot indicates the traditional 2DH friction formulation response and the blue dot the amplification under a phase shift of 45° . This figure shows that increasing the phase shift φ_a leads to lower responses (within the physical range). This is in contrast to section 4.3, where increasing the phase shift φ_a led to larger responses.

5. Discussion

Our results show that friction in a 3D model leads to inherently different results than friction in a 2DH model. In some cases, the result is that 2DH models cannot even be calibrated to approximate the 3D results properly as is illustrated in Section 4.3. This mismatch is primarily caused by the formation

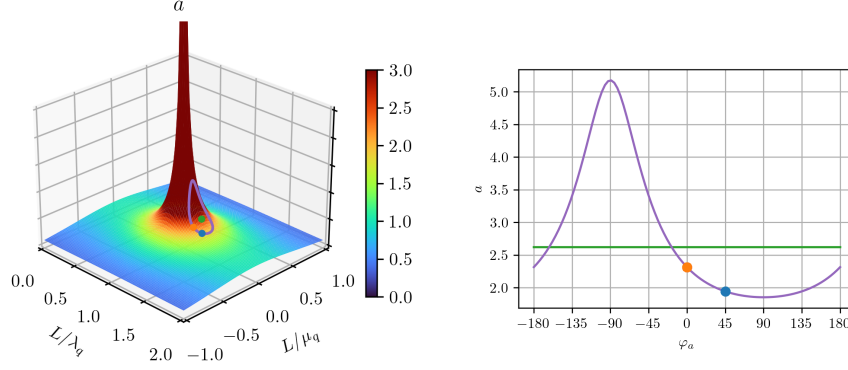


Figure 7: Left, amplification plane with a frictionless, 2DH friction and 3D friction formulation denoted by the green, orange and blue dots. The purple curve shows the effect of varying φ_a assuming it is a free parameter. Right, the amplification is plotted as a function of the phase shift φ_a , assuming it is a free parameter. The green line represents the frictionless amplification. The orange and blue dot indicate the amplification using the 2DH traditional and 3D friction formulation, respectively.

of a Stokes boundary layer near the bed. Such a layer is formed when both the Stokes number and the nondimensional parameter \mathcal{A} are small.

The difference between linearised depth-averaged and depth-resolving models stems from the difference between the near-bed and depth-averaged velocity, leading to different dissipation rates as a consequence of different bed shear stresses. In the literature various ideas have been put forward to explain the differences between depth-averaged and depth-resolving models. Firstly, the Coriolis effect causes the velocity to rotate over the vertical. This causes the near-bed tidal ellipse to be rotated with respect to the depth-averaged tidal ellipse and, as a consequence, the friction acts in a different direction than the depth-averaged velocity (Mofjeld, 1980). Secondly, since the depth-averaged velocity is generally larger than the near-bed velocity, it follows that it responds slower to changing pressure gradients, causing the near-bed velocity to lead the depth-averaged velocity. Therefore, the friction and depth-averaged velocity are out of phase (Vreugdenhil, 1994). Zielke (1966) showed that these effects differ for different frequencies. We, for the first time, show how to consistently combine these depth-resolving effects in a depth-averaged model such that the same depth-averaged dynamics as a depth-resolving model are recovered. This new parametrisation can be used in various geophysical systems, coastal seas and estuaries. Perhaps, this

parametrisation can even be used in atmospheric models.

The reduction from a linearised 3D model to a 2DH model is possible under certain assumptions on the flow. The velocities should be small enough and the length scales should be large enough such that advective terms can be neglected. For the bottom boundary condition, a linearised friction law is used. Another frequently used formulation is the quadratic bed shear stress. The non-linear nature of the quadratic friction law complicates the use of analytical solution techniques. Furthermore, the present model assumes a vertically uniform eddy viscosity formulation, which is generally considered to be a decent first approximation but more realistic vertical eddy viscosity profiles and turbulence models have been used. Different parametrisations of the eddy viscosity profiles, such as a parabolic profile, could lead to different near-bed velocities and therefore to different parametrisations of the near-bed velocity. These extensions might still be explained using the methods and concepts described in this paper.

6. Conclusion

In this paper, we have identified the differences in friction between a 3D and 2DH model and derived an exact friction formulation needed to reproduce the results of a linearised 3D model in a 2DH model. This required us to change the traditional friction parameter into a formulation that takes into account the past of the velocity signal. For harmonic signals, we have analysed in detail when these adaptations are important and this showed that it is especially important when the Stokes number is small. Furthermore, using the 3D friction formulation, a perfect match between the depth-averaged dynamics of two models is found, which was not possible under the traditional 2DH friction formulation. This indicates that the additional phase shift and cross-dependence of the friction terms can be important to correctly resolve the three-dimensional dynamics of the water motion.

Appendix A. The bed shear stress relation

In this section, the bed shear stress relation based on the 3D model is derived. Winant (2007) and Kumar et al. (2016) have shown how to solve the vertical structure of the velocity profile analytically for a single tidal constituent with angular frequency ω . Since this parameter plays a crucial role in our derivation, we make this parametric dependence explicit using

the notation ‘ ω ’. Furthermore, we have found that a matrix notation is preferable for clarity and brevity. The vertical analytical velocity in matrix notation in the frequency domain reads:

$$\mathbf{U}(x, y, z; \omega) = \mathbf{P} \mathbf{c}(x, y, z; \omega) \mathbf{P}^* \nabla Z(x, y; \omega),$$

with the constant unitary matrices and the vertical structure diagonal matrix for $\ell = 1, 2$ given by

$$\mathbf{P} = \frac{1}{\sqrt{2}} \begin{bmatrix} 1 & 1 \\ -i & i \end{bmatrix}, \quad \mathbf{P}^* = \frac{1}{\sqrt{2}} \begin{bmatrix} 1 & i \\ 1 & -i \end{bmatrix}, \quad c_{\ell\ell}(x, y, z; \omega) = \frac{g}{A_\nu \alpha_{\ell\ell}^2} \left\{ s_f \beta_{\ell\ell} \cosh(\alpha_{\ell\ell}(z - R)) - 1 \right\},$$

with the diagonal matrices

$$\alpha_{\ell\ell}(x, y; \omega) = \sqrt{\frac{i(\omega + (-1)^{\ell+1}f)}{A_\nu}}, \quad \beta_{\ell\ell}(x, y; \omega) = \frac{1}{A_\nu \alpha_{\ell\ell} \sinh(\alpha_{\ell\ell} D) + s_f \cosh(\alpha_{\ell\ell} D)}. \quad (\text{A.1})$$

Here, the subscript $\ell\ell$ denotes taking the ℓ th diagonal element of the 2×2 matrices.

To derive an exact parametrisation for the bed shear stress, an exact expression for the near-bed velocity and depth-averaged velocity are required. These can be obtained exactly since the vertical structure of the velocity profile is known analytically. The near-bed velocity is obtained by evaluating the vertical analytical velocity near the bed $z = -H$ and is given by

$$\mathbf{U}_b(x, y; \omega) = \mathbf{P} \mathbf{c}_b(x, y; \omega) \mathbf{P}^* \nabla Z(x, y; \omega),$$

with the vertical structure diagonal matrix evaluated near the bed $z = -H$ given by

$$c_{b,\ell\ell}(x, y; \omega) = \frac{g}{A_\nu \alpha_{\ell\ell}^2} \left\{ s_f \beta_{\ell\ell} \cosh(\alpha_{\ell\ell} D) - 1 \right\}.$$

The depth-averaged velocity is obtained by depth-averaging the vertical analytical velocity and reads

$$\bar{\mathbf{U}}(x, y; \omega) = \mathbf{P} \bar{\mathbf{c}}(x, y; \omega) \mathbf{P}^* \nabla Z(x, y; \omega),$$

with the depth-averaged diagonal matrix given by

$$\bar{c}_{\ell\ell}(x, y; \omega) = \frac{g}{A_\nu \alpha_{\ell\ell}^2} \left\{ \frac{s_f \beta_{\ell\ell}}{\alpha_{\ell\ell} D} \sinh(\alpha_{\ell\ell} D) - 1 \right\}.$$

The next step is using the exact expressions for the near-bed and depth-averaged velocity to obtain an exact parametrisation for the bed shear stress in the Fourier domain. We assume that there exists a complex-valued matrix \mathbf{R}^{3D} such that we may express the bed shear stress in the Fourier domain in terms of the depth-averaged velocity as

$$s_f(x, y) \mathbf{U}_b(x, y; \omega) = \mathbf{R}^{3D}(x, y; \omega) \overline{\mathbf{U}}(x, y; \omega). \quad (\text{A.2})$$

Substituting the exact expressions for the near-bed and depth-averaged velocities results in the following expression for the complex-valued friction matrix

$$\mathbf{R}^{3D}(x, y; \omega) = s_f(x, y) \mathbf{P} \Theta(x, y; \omega) \mathbf{P}^*, \quad (\text{A.3})$$

where we have defined the non-dimensional diagonal matrix

$$\Theta_{\ell\ell}(x, y; \omega) = \frac{c_{b,\ell\ell}(x, y; \omega)}{\bar{c}_{\ell\ell}(x, y; \omega)}.$$

This non-dimensional matrix turns out to be quite pivotal. It shows how to relate the 3D parameters to the 2DH parameters for harmonic signals.

Using Eq. (A.1) and some algebra, it is found that the elements of this non-dimensional matrix may be expressed as

$$\Theta_{\ell\ell}(x, y; \omega) = \frac{-\mathcal{A} \mathcal{D}_\ell^2}{1 - \mathcal{A} \mathcal{D}_\ell^2 - \frac{\mathcal{D}_\ell}{\tanh \mathcal{D}_\ell}}, \quad (\text{A.4})$$

where we have defined two non-dimensional parameters

$$\mathcal{A}(x, y) = \frac{A_\nu}{s_f D}, \quad \mathcal{D}_\ell(x, y; \omega) = \alpha_{\ell\ell} D.$$

The first non-dimensional parameter \mathcal{A} is the ratio between the vertical eddy viscosity A_ν and the product of the partial-slip parameter s_f and the depth D . This non-dimensional parameter may be derived from the partial-slip boundary condition. The second non-dimensional parameter is the product of the vertical decay length scale $\alpha_{\ell\ell}$ and the depth D . This non-dimensional parameter is complex-valued and its modules is inversely proportional to the Stokes number. Importantly, the second non-dimensional number depends on the frequency ω due to the frequency dependence of $\alpha_{\ell\ell}$.

For the computations, the complex nondimensional number \mathcal{D}_ℓ is used. However, for interpretation purposes we may write this complex number in polar form using two real-valued nondimensional parameters

$$\mathcal{D}_{1,2} = \frac{1}{\text{Stk}_\pm} \exp(i\pi/4\mathcal{P}_\pm),$$

with the real-valued nondimensional parameters given by

$$\text{Stk}_\pm(x, y; \omega) = \frac{1}{D} \sqrt{\frac{A_\nu}{|\omega \pm f|}}, \quad \mathcal{P}_\pm = \text{sign}(\omega \pm f).$$

The index $\ell = 1$ corresponds to the $+$ sign and the index $\ell = 2$ corresponds to the $-$ sign.

The elements of the 3D friction matrix are found by expanding the matrices in Eq. (A.3) and this yields

$$\mathbf{R}^{3\text{D}}(x, y; \omega) = s_f \frac{1}{2} \begin{bmatrix} \Theta_{11} + \Theta_{22} & i(\Theta_{11} - \Theta_{22}) \\ -i(\Theta_{11} - \Theta_{22}) & \Theta_{11} + \Theta_{22} \end{bmatrix}. \quad (\text{A.5})$$

The elements of this matrix can be expressed in polar form as

$$\mathbf{R}^{3\text{D}}(x, y; \omega) = s_f \begin{bmatrix} r_1 e^{i\varphi_1} & -r_2 e^{i\varphi_2} \\ r_2 e^{i\varphi_2} & r_1 e^{i\varphi_1} \end{bmatrix}, \quad (\text{A.6})$$

where we have defined the amplitudes and phases

$$\begin{aligned} r_1 &= \frac{1}{2} |\Theta_{11} + \Theta_{22}|, & r_2 &= \frac{1}{2} |\Theta_{11} - \Theta_{22}|, \\ \varphi_1 &= \arg(\Theta_{11} + \Theta_{22}), & \varphi_2 &= -\frac{\pi}{2} + \arg(\Theta_{11} - \Theta_{22}). \end{aligned}$$

No Coriolis

The 3D friction matrix simplifies in case there is no Coriolis force: $f = 0$. In this case, the coefficient $\alpha_{\ell\ell}$ becomes independent of the index ℓ , thus $\alpha_{11} = \alpha_{22}$. Since all the other coefficients only depend on the index ℓ through the $\alpha_{\ell\ell}$'s, it follows that all coefficients become ℓ independent. As a consequence, we have $\Theta_{11} = \Theta_{22}$ and, therefore,

$$\mathbf{R}^{3\text{D}}(x, y; \omega) = s_f \begin{bmatrix} \Theta_{11} & 0 \\ 0 & \Theta_{11} \end{bmatrix} = s_f \Theta_{11} \mathbf{I}_2.$$

The polar form of its elements simplifies to

$$r_1 = |\Theta_{11}|, \quad r_2 = 0, \quad \varphi_1 = \arg(\Theta_{11}), \quad \varphi_2 = -\frac{\pi}{2}.$$

The relevant parameters in this case are r_1 and φ_1 . The parameter φ_2 is not relevant in the no Coriolis case since $r_2 = 0$.

References

- Batchelor, G.K., 1967. An introduction to fluid dynamics. Cambridge University Press, Cambridge.
- Chekhova, M., Banzer, P., 2021. Polarization of Light In Classical, Quantum, and Nonlinear Optics. De Gruyter.
- Cushman-Roisin, B., Beckers, J.M., 2009. Introduction to Geophysical Fluid Dynamics: Physical and Numerical Aspects. Academic Press.
- Defant, A., 1961. Physical oceanography. Pergamon, New York.
- Dyer, K.R., 1974. The salt balance in stratified estuaries. *Estuarine and Coastal Marine Science* 2, 273–281. doi:10.1016/0302-3524(74)90017-6.
- Fischer, H.B., 1972. Mass transport mechanisms in partially stratified estuaries. *Journal of Fluid Mechanics* 53, 671–687. doi:10.1017/S0022112072000412.
- Friedrichs, C.T., 2010. Barotropic tides in channelized estuaries, in: Valle-Levinson, A. (Ed.), *Contemporary Issues in Estuarine Physics*. Cambridge University Press, Cambridge. chapter 3, pp. 27–61. doi:10.1017/CB09780511676567.
- Garrett, C., 1975. Tides in gulfs. *Deep-Sea Research and Oceanographic Abstracts* 22, 23–35. doi:10.1016/0011-7471(75)90015-7.
- Glock, K., Tritthart, M., Habersack, H., Hauer, C., 2019. Comparison of hydrodynamics simulated by 1D, 2D and 3D models focusing on bed shear stresses. *Water* 11, 30–37. doi:10.3390/w11020226.
- Hulscher, S.J., 1996. Tidal-induced large-scale regular bed form patterns in a three-dimensional shallow water model. *Journal of Geophysical Research: Oceans* 101, 20727–20744. doi:10.1029/96JC01662.

- Huthnance, J.M., 1980. On shelf-sea ‘resonance’ with application to Brazilian M3 tides. *Deep Sea Research Part A, Oceanographic Research Papers* 27, 347–366. doi:10.1016/0198-0149(80)90031-X.
- Kumar, M., Schuttelaars, H.M., Roos, P.C., Möller, M., 2016. Three-dimensional semi-idealized model for tidal motion in tidal estuaries: An application to the Ems estuary. *Ocean Dynamics* 66, 99–118. doi:10.1007/s10236-015-0903-1.
- Li, C., O’Donnell, J., 1997. Tidally driven residual circulation in shallow estuaries with lateral depth variation. *Journal of Geophysical Research C: Oceans* 102, 27915–27929. doi:10.1029/97JC02330.
- Marinone, S.G., 2000. Tidal currents in the Gulf of California: Intercomparisons among two- and three-dimensional models with observations. *Ciencias Marinas* 26, 275–301. doi:10.7773/cm.v26i2.579.
- Mofjeld, H.O., 1980. Effects of Vertical Viscosity on Kelvin Waves. *Journal of Physical Oceanography* 10, 1039–1050. doi:10.1175/1520-0485(1980)010<1039:eovvok>2.0.co;2.
- Prandle, D., 1982. The vertical structure of tidal currents. *Geophysical & Astrophysical Fluid Dynamics* 22, 29–49. doi:10.1080/03091928208221735.
- Roos, P.C., Velema, J.J., Hulscher, S.J., Stolk, A., 2011. An idealized model of tidal dynamics in the North Sea: Resonance properties and response to large-scale changes. *Ocean Dynamics* 61, 2019–2035. doi:10.1007/s10236-011-0456-x.
- Schramkowski, G.P., De Swart, H.E., 2002. Morphodynamic equilibrium in straight tidal channels: Combined effects of Coriolis force and external overtides. *Journal of Geophysical Research: Oceans* 107. doi:10.1029/2000jc000693.
- Schramkowski, G.P., Schuttelaars, H.M., Swart, H.E.D., 2002. The effect of geometry and bottom friction on local bed forms in a tidal embayment. *Continental Shelf Research* 22, 1821–1833.
- Soulsby, R.L., 1981. Measurements of the Reynolds stress components close to a marine sand bank. *Marine Geology* 42, 35–47. doi:10.1016/0025-3227(81)90157-2.

- Soulsby, R.L., 1983. The bottom boundary layer of shelf seas, in: Johns, B. (Ed.), *Physical Oceanography of Coastal and Shelf Seas*. Elsevier, Amsterdam.
- Souza, A.J., 2013. On the use of the Stokes number to explain frictional tidal dynamics and water column structure in shelf seas. *Ocean Science* 9, 391–398. doi:10.5194/os-9-391-2013.
- Souza, A.J., Simpson, J.H., 1996. The modification of tidal ellipses by stratification in the Rhine ROFI. *Continental Shelf Research* 16, 997–1007. doi:10.1016/0278-4343(95)00042-9.
- Stacey, M.T., Burau, J.R., Monismith, S.G., 2001. Creation of residual flows in a partially stratified estuary. *Journal of Geophysical Research: Oceans* 106, 17013–17037. doi:10.1029/2000JC000576.
- Taylor, G.I., 1922. Tidal oscillations in gulfs and rectangular basins. *Proceedings of the London Mathematical Society* s2-20, 148–181.
- Van Rijn, L.C., 2010. Tidal phenomena in the Scheldt Estuary. Technical Report. Deltares. URL: <http://www.vliz.be/imisdocs/publications/214759.pdf>.
- Vreugdenhil, C.B., 1994. *Numerical methods for shallow-water flow*. Kluwer Academic Publishers, Dordrecht. doi:10.1007/978-94-015-8354-1.
- Winant, C.D., 2007. Three-dimensional tidal flow in an elongated, rotating basin. *Journal of Physical Oceanography* 37, 2345–2362. doi:10.1175/JPO3122.1.
- Wong, K.C., 1994. On the nature of transverse variability in a coastal plain estuary. *Journal of Geophysical Research* 99, 14209. doi:10.1029/94JC00861.
- Zielke, W., 1966. Frequency dependent friction in transient pipe flow. Phd dissertation. University of Michigan.

Electronic Supplement: The relationship between linearised 3D and 2DH models for tidally dominated shallow waters

Journal: Ocean Modelling

Authors: Marco P. Rozendaal, Yoei M. Dijkstra, and Henk M. Schuttelelaars

Affiliation: Delft Institute of Applied Mathematics, Delft University of Technology, Delft, The Netherlands

E-mail: M.P.Rozendaal@tudelft.nl

Appendix B. Tidal ellipse parameters

Interpreting the 3D friction formulation (A.5) in the form given by equation (A.6) turns out to be quite difficult. A physically more intuitive description of the 3D friction formulation can be obtained by considering the tidal ellipse, which is the ellipse traced out by the velocity vector over a tidal cycle. The parameters characterising the ellipse can conveniently be expressed in terms of the rotating flow variables. The Cartesian velocity can be converted to rotating flow variables as

$$\mathbf{R} = \mathbf{P}^* \mathbf{U},$$

where the amplitude of first component of the rotating flow variables $|R_1|$ indicates the importance of the anticlockwise rotation and the amplitude of the second component $|R_2|$ the clockwise rotation. To see this, associate the horizontal velocity vector u, v to the complex velocity plane as $w = u + iv$, with u and v real-valued. Substituting the single component Fourier expansion (11) and using the rotating flow variables yields

$$w = u + iv = R_1 \frac{1}{\sqrt{2}} e^{i\omega t} + R_2^* \frac{1}{\sqrt{2}} e^{-i\omega t},$$

with the star $*$ denoting complex conjugation.

We describe the tidal ellipse using 5 parameters:

- the magnitude of the semi-major axis: M ;
- the *signed* magnitude of the semi-minor axis: m . Positive indicates anticlockwise rotation, negative indicates clockwise rotation;

- the orientation of the ellipse (the angle of the semi-major axis with respect to the x -axis): θ ;
- the phase of the ellipse (the phase difference between reaching the maximal tidal current and $\omega t = 0$): ψ ;
- the *signed* ellipticity ε . For $\varepsilon = 0$, the ellipse becomes a degenerate (a line). For $|\varepsilon| = 1$, the ellipse is a circle. Positive indicates anticlockwise rotation, negative indicates clockwise rotation.

The tidal ellipse parameters expressed in terms of the rotating flow variables read (see, e.g., Souza and Simpson, 1996)

$$\begin{aligned} M &= \frac{1}{\sqrt{2}}(|R_1| + |R_2|), & m &= \frac{1}{\sqrt{2}}(|R_1| - |R_2|), & \varepsilon &= \frac{m}{M}, \\ \theta &= \frac{1}{2}(\phi_1 + \phi_2), & \psi &= -\frac{1}{2}(\phi_1 - \phi_2), \end{aligned}$$

where we have defined the phases:

$$\phi_1 = \arg(R_1), \quad \phi_2 = -\arg(R_2).$$

Here, we have taken into account that our rotating flow variables are scaled with the factor $\sqrt{2}$ and the complex conjugation of the second rotating flow variable results in the minus sign of ϕ_2 .

The 3D friction formulation may be interpreted as the relation between the near-bed velocity and the depth-averaged velocity apart from a factor s_f . Multiplying this relation (A.2) from the left with \mathbf{P}^* and cancelling the factors s_f results in

$$\mathbf{P}^* \mathbf{U}_b(x, y; \omega) = \mathbf{\Theta}(x, y; \omega) \mathbf{P}^* \overline{\mathbf{U}}(x, y; \omega).$$

We define the rotating flow variables for both the near-bed and depth-averaged velocity, to obtain

$$\mathbf{R}_b(x, y; \omega) = \mathbf{\Theta}(x, y; \omega) \overline{\mathbf{R}}(x, y; \omega).$$

Here is $\mathbf{\Theta}$ a diagonal matrix. So, we have component wise:

$$\begin{cases} R_{b,1} = \Theta_{11} \overline{R}_1, \\ R_{b,2} = \Theta_{22} \overline{R}_2. \end{cases}$$

The rotating flow variables of the near-bed velocity and depth-averaged velocity have their own tidal ellipse parameters. Using the relationships defined above, we can express the near-bed tidal ellipse parameters in terms of the depth-averaged tidal ellipse parameters as

$$\begin{aligned} M_b &= \bar{M}r_a(1 + \bar{\varepsilon}r_r), \\ m_b &= \bar{M}r_a(\bar{\varepsilon} + r_r), \\ \theta_b &= \bar{\theta} + \varphi_d, \\ \psi_b &= \bar{\psi} - \varphi_a, \\ \varepsilon_b &= \frac{m_b}{M_b} = \frac{\bar{\varepsilon} + r_r}{1 + \bar{\varepsilon}r_r}. \end{aligned}$$

Here, we have defined the dimensionless amplitudes and phases (with the subscript denoting average, deviation and ratio):

$$r_a = \frac{|\Theta_{11}| + |\Theta_{22}|}{2}, \quad r_d = \frac{|\Theta_{11}| - |\Theta_{22}|}{2}, \quad r_r = \frac{r_d}{r_a}, \quad (\text{B.1})$$

$$\varphi_a = \frac{\arg(\Theta_{11}) + \arg(\Theta_{22})}{2}, \quad \varphi_d = \frac{\arg(\Theta_{11}) - \arg(\Theta_{22})}{2}. \quad (\text{B.2})$$

No Coriolis

If there is no Coriolis force, $f = 0$, the tidal ellipse parameters of the near-bed velocity simplify. Again, it follows that $\Theta_{11} = \Theta_{22}$ for $f = 0$, such that the nondimensional amplitudes and phases become

$$r_a = |\Theta_{11}|, \quad r_d = 0, \quad r_r = 0, \quad \varphi_a = \arg(\Theta_{11}), \quad \varphi_d = 0.$$

The near-bed tidal ellipse parameters then read

$$M_b = \bar{M}r_a, \quad m_b = \bar{\varepsilon}\bar{M}r_a = \bar{m}r_a, \quad \theta_b = \bar{\theta}, \quad \psi_b = \bar{\psi} - \varphi_a, \quad \varepsilon_b = \bar{\varepsilon}.$$

Appendix C. Boundary layer solution

We solve the 3D hydrodynamic equations in the small $\text{Stk} \ll 1$ limit. We assume there is no Coriolis force. We derive the corresponding nondimensional variables, the boundary layer solution and the composite solution.

We assume the dimensional variables can be written as a characteristic scale times a nondimensional number denoted with the $*$ as follows

$$\mathbf{u} = U\mathbf{u}^*, \quad t = \frac{1}{\omega}t^*, \quad \zeta = A\zeta^*, \quad \mathbf{x} = L\mathbf{x}^*, \quad z = Dz^*.$$

Substitution into the 3D momentum equations (3) and dividing by ωU yields

$$\mathbf{u}_{t*}^* = -\frac{gA}{\omega UL} \nabla^* \zeta^* + \text{Stk}^2 \mathbf{u}_{z*}^*.$$

We define the velocity scale as $U = gA/(\omega L)$ and we omit the nondimensional symbol $*$, to obtain

$$\mathbf{u}_t = -\nabla \zeta + \text{Stk}^2 \mathbf{u}_{zz}.$$

Similarly, the nondimensional no-stress (4) and partial-slip (5) conditions are written in terms of nondimensional quantities. For simplicity, we assume $R = 0$ and $D = H$, to get

$$\mathbf{u}_z = 0, \quad \text{at } z = 0, \quad \mathcal{A}\mathbf{u}_z = \mathbf{u}_b, \quad \text{at } z = -1.$$

Hence, the nondimensional vertical scale ranges from $z = -1$ at the bed to $z = 0$ at the free surface.

Since the forcing is harmonic and the equation is linear, we seek a nondimensional solution with the same periodicity

$$\mathbf{u}(t) = \Re\{\mathbf{U}e^{it}\}, \quad \zeta(t) = \Re\{Ze^{it}\}.$$

This results in the following equation

$$i\mathbf{U} = -\nabla Z + \text{Stk}^2 \mathbf{U}_{zz},$$

with boundary conditions

$$\mathbf{U}_z = 0, \quad \text{at } z = 0, \quad \mathcal{A}\mathbf{U}_z = \mathbf{U}_b, \quad \text{at } z = -1.$$

For small $\text{Stk} \ll 1$, the above equation is singularly perturbed, indicating that a boundary layer might be formed. We note that this equation can still be solved analytically, but the solution obtained using singular perturbation theory may offer some additional insights. The small perturbation parameter is $\text{Stk} \ll 1$. Assume we may expand outer solution in Stk as

$$\hat{\mathbf{U}} = \hat{\mathbf{U}}^0 + \text{Stk} \hat{\mathbf{U}}^1 + \dots$$

Substitution in to the above equation and collection like powers of Stk yields at leading-order $\mathcal{O}(\text{Stk}^0)$:

$$\hat{\mathbf{U}}^0 = i\nabla Z.$$

Since Z does not depend on the vertical coordinate z , it follows that $\hat{\mathcal{U}}^0$ does not depend on the vertical coordinate z . We see that we directly satisfy the boundary condition at the free surface $z = 0$. To satisfy the boundary condition near the bed, a boundary layer is formed. In this layer, the dominant balance is different than in the outer domain. So we assume there exists a small layer near the bed and we define the new coordinate

$$\tilde{z} = \frac{z + 1}{\text{Stk}^\alpha},$$

for $0 \leq \tilde{z} < \infty$. We call the solution in the boundary layer $\mathcal{U}(\tilde{z})$. Substitution into the equation and transforming coordinates yields

$$i\mathcal{U} = -\nabla Z + \text{Stk}^{2-2\alpha} \mathcal{U}_{\tilde{z}\tilde{z}},$$

The only balance that can be formed in the boundary layer that includes the second derivative is given by $\alpha = 1$, which is a dominant balance. In the boundary layer all three terms are equally important. We also expand write the partial-slip condition in terms of the new coordinate

$$\frac{\mathcal{A}}{\text{Stk}} \mathcal{U}_{\tilde{z}} = \mathcal{U}_b \quad \text{at} \quad \tilde{z} = 0.$$

Also expanding the inner solution in a series in Stk yields

$$\mathcal{U} = \mathcal{U}^0 + \text{Stk} \mathcal{U}^1 + \dots$$

Collecting the leading order terms in the boundary layer yields

$$i\mathcal{U}^0 = -\nabla Z + \mathcal{U}_{\tilde{z}\tilde{z}}^0,$$

The general solution of this ode with constant coefficients is given by

$$\mathcal{U}^0(z) = \mathbf{A}e^{\sqrt{i}\tilde{z}} + \mathbf{B}e^{-\sqrt{i}\tilde{z}} + i\nabla Z,$$

with vectors \mathbf{A} and \mathbf{B} . Applying the partial-slip condition yields

$$\mathbf{B} = -\frac{1 - \sqrt{i}\mathcal{A}/\text{Stk}}{1 + \sqrt{i}\mathcal{A}/\text{Stk}} \mathbf{A} - \frac{1}{1 + \sqrt{i}\mathcal{A}/\text{Stk}} i\nabla Z.$$

We apply the simple matching rule that states that the outer solution approaching the boundary layer should be the same as the inner solution leaving the boundary layer:

$$\lim_{z \rightarrow -1} \hat{\mathbf{U}}^0(z) = \lim_{\tilde{z} \rightarrow \infty} \mathbf{U}^0(\tilde{z}).$$

This condition requires that $\mathbf{A} = \mathbf{0}$ and the matching condition is satisfied. The boundary layer solution is thus

$$\mathbf{U}^0(\tilde{z}) = i \left(1 - \frac{1}{1 + \sqrt{i}\mathcal{A}/\text{Stk}} e^{-\sqrt{i}\tilde{z}} \right) \nabla Z.$$

Since the outer solution is constant, the composite solution simplifies to just the inner solution expressed in terms of the z coordinate:

$$\mathbf{U} = \hat{\mathbf{U}}^0 + \mathbf{U}^0 - \hat{\mathbf{U}}^0(-1) = i \left(1 - \frac{1}{1 + \sqrt{i}\mathcal{A}/\text{Stk}} e^{-\sqrt{i}(z+1)/\text{Stk}} \right) \nabla Z.$$

We want to compute the phase difference between the near-bed velocity and the depth-averaged velocity. In case there is no Coriolis force we may write

$$\mathbf{U}_b = r_a e^{i\varphi_a} \overline{\mathbf{U}}.$$

Taking the arguments (element wise) and rearranging yields

$$\varphi_a \mathbf{1} = \arg(\mathbf{U}_b) - \arg(\overline{\mathbf{U}}),$$

where $\mathbf{1}$ is a vector with only ones.

In the limit $\text{Stk} \rightarrow 0$, we have that the depth-averaged velocity goes to the depth-averaged outer solution. Since the outer solution is constant in z , it follows that this is the same as the outer solution itself. Hence,

$$\overline{\mathbf{U}} \rightarrow \overline{\hat{\mathbf{U}}^0} = \hat{\mathbf{U}}^0.$$

Then we have for phase difference between the near-bed and the depth-averaged velocity that

$$\varphi_a \mathbf{1} = \arg \lim_{\tilde{z} \rightarrow 0} \mathbf{U}^0(\tilde{z}) - \arg \hat{\mathbf{U}}^0 = \arg \left(1 - \frac{1}{1 + \sqrt{i}\mathcal{A}/\text{Stk}} \right) \mathbf{1} = \arctan \left(\frac{1}{1 + \sqrt{2}\mathcal{A}/\text{Stk}} \right) \mathbf{1}.$$

Furthermore, since the outer solution is constant over the depth, it follows that its phase is also constant over the depth. Thus, the phase difference φ_a must be due to a phase difference between the near-bed velocity and the velocity just above the boundary layer. This shows that the phase difference between the near-bed velocity and the depth-averaged velocity φ_a is acquired over the thin boundary layer and not over the whole depth.

Appendix D. Amplification

One of the key differences between the new and traditional friction formulation is the inclusion of the phase shift between the near-bed and the depth-averaged velocity, φ_a . To study its importance, we consider a narrow rectangular estuary with uniform across and along-channel parameters. We set the Coriolis force to zero. At the seaward side $x = 0$, we prescribe a laterally uniform M_2 amplitude. At the landward side $x = L$ and at the lateral sides $y = 0$ and $y = B$, a no-transport boundary is imposed. Under these conditions the depth-averaged shallow water equations in the frequency domain read (see, Eq. (12))

$$\begin{cases} i\omega Z + (D\bar{U})_x + (D\bar{V})_y = 0, \\ i\omega\bar{U} = -gZ_x - \frac{1}{D}s_fr_a e^{i\varphi_a}\bar{U}, \\ i\omega\bar{V} = -gZ_y - \frac{1}{D}s_fr_a e^{i\varphi_a}\bar{V}, \end{cases} \quad (\text{D.1})$$

where we have used that under the 3D friction formulation without Coriolis, one has

$$\mathbf{U}_b = r_a e^{i\varphi_a} \bar{\mathbf{U}}.$$

Solving for the velocity vector yields

$$\bar{\mathbf{U}} = \frac{i\omega}{D} \frac{1}{\kappa^2} \nabla Z.$$

Here, we have defined the complex wavenumber as

$$\kappa = \kappa_0 \gamma, \quad \kappa_0 = \frac{\omega}{\sqrt{gD}}, \quad \gamma = \sqrt{1 + \frac{s_fr_a}{i\omega D} e^{i\varphi_a}}.$$

For $s_fr_a = 0$, we recover the frictionless case with $\gamma = 1$ and the frictionless wavenumber $\kappa = \kappa_0$. For $\varphi_a = 0$, the traditional friction formulation is recovered. Thus the 3D friction formulation includes both the frictionless and traditional friction formulation as special cases.

Substituting into the depth-integrated continuity equation and using that the parameters are spatially constant yields a Helmholtz equation for Z :

$$\Delta Z + \kappa^2 Z = 0.$$

Using that the prescribed M_2 forcing has no lateral structure, the exact solution can be found using separation of variables as

$$Z(x, y) = \frac{A}{\cos(\kappa L)} \cos(\kappa(x - L)),$$

with A the prescribed amplitude. Since Z has no lateral structure, i.e., is constant in y , we write $Z(x, y) = Z(x)$.

A useful metric to measure the amplification within an estuary is to define the amplification factor as the ratio between the amplitude at the landward side and the prescribed amplitude at the seaward side:

$$a = \frac{|Z(L)|}{|Z(0)|} = \frac{1}{|\cos \kappa L|}.$$

Appendix E. Deriving the relationship between 3D and 2DH models

In this section, we derive the relationship between 3D and 2DH models for general time signals. For this we need the temporal Fourier transform. We use the following convention. We define the Fourier transform as

$$F(\omega) = \mathcal{F}\{f(t)\}(\omega) = \int_{-\infty}^{\infty} f(t)e^{-i\omega t} dt,$$

and the inverse Fourier transform as

$$f(t) = \mathcal{F}^{-1}\{F(\omega)\}(t) = \frac{1}{2\pi} \int_{-\infty}^{\infty} F(\omega)e^{i\omega t} d\omega.$$

The 2DH hydrodynamic equations are linear in the unknowns, hence applying the Fourier transform yields

$$\begin{cases} i\omega Z + (D\bar{U})_x + (D\bar{V})_y = 0, \\ i\omega\bar{U} - f\bar{V} = -gZ_x - \frac{1}{D}s_f U_b, \\ i\omega\bar{V} + f\bar{U} = -gZ_y - \frac{1}{D}s_f V_b. \end{cases}$$

where we have defined the Fourier transformed quantities

$$\begin{bmatrix} Z \\ \bar{U} \\ \bar{V} \\ U_b \\ V_b \end{bmatrix} (x, y, \omega) = \mathcal{F} \left\{ \begin{bmatrix} \zeta \\ \bar{u} \\ \bar{v} \\ u_b \\ v_b \end{bmatrix} (x, y, t) \right\} (x, y, \omega).$$

We note that these are the same equations as we have obtained when we considered a single frequency ω in the case of a harmonic signal. The difference is that these hold for all frequencies ω in \mathbb{R} .

The bed shear stress relation derived for a single harmonic constituent Eq. (A.2) is, in fact, valid for each frequency ω . Thus using it for all frequencies, we are able to express the near-bed velocity in terms of the depth-averaged velocity in the frequency domain:

$$s_f \mathbf{U}_b(x, y, \omega) = \mathbf{R}^{3D}(x, y, \omega) \bar{\mathbf{U}}(x, y, \omega). \quad (\text{E.1})$$

The last step in the derivation is transforming back to the time domain using the inverse Fourier transform. We obtain the equivalent 2DH equations

$$\begin{cases} \zeta_t + (D\bar{u})_x + (D\bar{v})_y = 0, \\ \bar{u}_t - f\bar{v} = -g\zeta_x - \frac{1}{D}s_f u_b, \\ \bar{v}_t + f\bar{u} = -g\zeta_y - \frac{1}{D}s_f v_b. \end{cases}$$

It appears we have done nothing, but, in fact, we have found an explicit expression for the near-bed velocity in terms of the depth-averaged velocity in the Fourier domain. Taking the inverse Fourier transform of equation (E.1), shows that

$$s_f \mathbf{u}_b(x, y, t) = \mathcal{F}^{-1} \{ \mathbf{R}^{3D}(x, y, \omega) \bar{\mathbf{U}}(x, y, \omega) \} (x, y, t).$$

The inverse Fourier transform of a product of two functions is equal to the convolution of their inverse Fourier transforms by the Convolution theorem. Since the inverse Fourier transform is linear, this theorem can be used for each element of the matrix vector product, i.e., it is used element wise. Thus we find

$$s_f \mathbf{u}_b(x, y, t) = (\mathbf{r}^{3D} * \bar{\mathbf{u}})(x, y, t), \quad (\text{E.2})$$

where we have defined the inverse Fourier transform of the 3D friction matrix

$$\mathbf{r}^{3D}(x, y, t) = \mathcal{F}^{-1} \{ \mathbf{R}^{3D}(x, y, \omega) \} (x, y, t), \quad (\text{E.3})$$

and the symbol $*$ denotes the convolution and is defined as

$$(f * g)(t) = \int_{-\infty}^{\infty} f(\tau) g(t - \tau) d\tau.$$

Since the convolution operator is distributive, we can define it to work on each element of a matrix vector product individually, i.e., the convolution operator also works element wise.

Since the inverse Fourier transform is a linear operator, we can simplify the inverse Fourier transform using equation (A.3) to

$$\mathbf{r}^{3D}(x, y, t) = s_f(x, y) \mathbf{P} \boldsymbol{\theta}(x, y, t) \mathbf{P}^*, \quad (\text{E.4})$$

where we have defined the inverse Fourier transform of the diagonal matrix Eq. (A.4) as

$$\boldsymbol{\theta}(x, y, t) = \mathcal{F}^{-1} \{ \boldsymbol{\Theta}(x, y, \omega) \} (x, y, t).$$

In Appendix F, the inverse Fourier transform of the diagonal matrix $\boldsymbol{\Theta}(x, y, \omega)$ is computed.

Appendix F. The inverse Fourier transform

In this section, we consider for $\ell = 1, 2$ the following inverse Fourier transform

$$\theta_{\ell\ell}(x, y, t) = \mathcal{F}^{-1} \{ \Theta_{\ell\ell}(x, y, \omega) \} (x, y, t).$$

We first consider a special case. For $\mathcal{A} \rightarrow 0$, we find $\Theta_{\ell\ell}(x, y, \omega) \rightarrow 0$. The inverse Fourier transform for $\mathcal{A} = 0$ becomes

$$\theta_{\ell\ell}(x, y, t) = 0.$$

In the following sections, we consider the general case where $\mathcal{A} > 0$. We are going to define several new variables to make the inversion more streamlined. The function $\Theta_{\ell\ell}(x, y, \omega)$ does not decay for $\omega \rightarrow \pm\infty$. We separate $\Theta_{\ell\ell}(x, y, \omega)$ into a non-decaying and decaying part as

$$\Theta_{\ell\ell}(x, y, \omega) = 1 - G(\mathcal{D}_\ell(\omega)),$$

where we have defined the decaying part as

$$G(\mathcal{D}_\ell(\omega)) = \frac{1 - \frac{\mathcal{D}_\ell}{\tanh \mathcal{D}_\ell}}{1 - \mathcal{A}\mathcal{D}_\ell^2 - \frac{\mathcal{D}_\ell}{\tanh \mathcal{D}_\ell}}.$$

We omit the spatial dependence of $\mathcal{D}_\ell(\omega)$ for notational convenience. From now on, we may omit the spatial dependency of a variable.

Since the inverse Fourier transform is linear it follows that

$$\theta_{\ell\ell}(x, y, t) = \delta(t) - g_\ell(x, y, t),$$

where we have defined

$$g_\ell(x, y, t) = \mathcal{F}^{-1}\{G(\mathcal{D}_\ell(\omega))\}.$$

We notice that the only ω dependence of $G(\mathcal{D}_\ell(\omega))$ is through $\mathcal{D}_\ell(\omega)$. We define the new variable

$$\mathcal{D}(\omega) = \sqrt{i\omega},$$

and notice that

$$\mathcal{D}_\ell(\omega) = \mathcal{D}\left(\frac{\omega - (-1)^\ell f}{\sigma}\right).$$

Here, we have defined the (vertical) frequency scale

$$\sigma(x, y) = \frac{A_\nu}{D^2}.$$

Thus, we have using the shift and scaling properties of the inverse Fourier transform that

$$\begin{aligned} g_\ell(x, y, t) &= \mathcal{F}^{-1}\left\{G\left[\mathcal{D}\left(\frac{\omega - (-1)^\ell f}{\sigma}\right)\right]\right\} \\ &= \exp((-1)^\ell ift) \mathcal{F}^{-1}\left\{G\left[\mathcal{D}\left(\frac{\omega}{\sigma}\right)\right]\right\} \\ &= \exp((-1)^\ell ift) \sigma g(x, y, \sigma t). \end{aligned}$$

where we have defined the inverse Fourier transform

$$g(x, y, t) = \mathcal{F}^{-1}\{G[\mathcal{D}(\omega)]\}(x, y, t).$$

So, we have successfully removed the ℓ and σ dependence from the inverse Fourier transform.

We summarise what we have found so far for $\mathcal{A} > 0$. We have derived that we can express the inverse Fourier transform for $\ell = 1, 2$ as

$$\theta_{\ell\ell}(t) = \delta(t) - \exp((-1)^\ell i f t) \sigma g(\sigma t).$$

This form already contains some interesting properties. To fully appreciate them, we use the three-dimensional friction matrix given by equation (E.4) and expand it, to obtain

$$\mathbf{r}^{3D}(x, y, t) = s_f \frac{1}{2} \begin{bmatrix} \theta_{11} + \theta_{22} & i(\theta_{11} - \theta_{22}) \\ -i(\theta_{11} - \theta_{22}) & \theta_{11} + \theta_{22} \end{bmatrix}.$$

This is completely analogous to the frequency domain formulation given in equation (A.5). This was to be expected as these matrices are Fourier transform pairs, see (E.3).

Using the above, it follows that

$$\mathbf{r}^{3D}(x, y, t) = s_f \begin{bmatrix} \delta(t) - \cos(ft) \sigma g(\sigma t) & -\sin(ft) \sigma g(\sigma t) \\ \sin(ft) \sigma g(\sigma t) & \delta(t) - \cos(ft) \sigma g(\sigma t) \end{bmatrix}.$$

This can be compactly written as

$$\mathbf{r}^{3D}(x, y, t) = s_f (\delta(t) \mathbf{I}_2 - \sigma g(\sigma t) \mathbf{R}^T(ft)).$$

Here, we have defined the 2×2 identity matrix and the clockwise rotation matrix over an angle ft as

$$\mathbf{I}_2 = \begin{bmatrix} 1 & 0 \\ 0 & 1 \end{bmatrix}, \quad \mathbf{R}^T(ft) = \begin{bmatrix} \cos(ft) & \sin(ft) \\ -\sin(ft) & \cos(ft) \end{bmatrix}.$$

Expanding the convolutional bed shear stress relation, Eq. (E.2), shows that

$$s_f \mathbf{u}_b(x, y, t) = s_f (\bar{\mathbf{u}}(t) - (\sigma g(\sigma t) \mathbf{R}^T(ft) * \bar{\mathbf{u}})(t)).$$

The second term can be written as

$$\sigma g(\sigma t) \mathbf{R}^T(ft) = \begin{bmatrix} h_1(t) & h_2(t) \\ -h_2(t) & h_1(t) \end{bmatrix},$$

where we have defined the history kernels

$$h_1(t) = \sigma g(\sigma t) \cos(ft), \quad h_2(t) = \sigma g(\sigma t) \sin(ft). \quad (\text{F.1})$$

Using the residue theorem, it will become clear why we call these functions history kernels, see equation (F.10) for details. These are the functions found in the equivalent 2DH equations for general time signals, see equation (16).

Appendix F.1. The Residue theorem

In this section, an analytical expression for g is derived using the residue theorem for $\mathcal{A} > 0$. Writing out the inverse Fourier transform yields

$$g(x, y, t) = \frac{1}{2\pi} \int_{-\infty}^{\infty} f(\omega) d\omega,$$

where we have defined the integrand

$$f(\omega) = G(\mathcal{D}(\omega)) \exp(i\omega t) = \frac{1 - \frac{\sqrt{i\omega}}{\tanh \sqrt{i\omega}}}{1 - \mathcal{A}i\omega - \frac{\sqrt{i\omega}}{\tanh \sqrt{i\omega}}} \exp(i\omega t).$$

We want to evaluate this integral using the Residue theorem. Thus we now allow our angular frequency ω to be complex valued.

The residue theorem states that

$$\oint_{\gamma} f(\omega) d\omega = 2\pi i \sum_k \text{Res}(f, z_k),$$

where the sum runs over all poles z_k inside of the positively orientated simple closed curve γ .

We define the sequence of functions

$$g_n(x, y, t) = \frac{1}{2\pi} \int_{-R_n}^{R_n} f(\omega) d\omega,$$

where R_n is a sequence of real-valued positive numbers for $n = 1, 2, 3, 4, \dots$ that tends to infinity as n tends to infinity, i.e., $\lim_{n \rightarrow \infty} R_n \rightarrow \infty$. We see that we recover our original function in the limit:

$$g(x, y, t) = \lim_{n \rightarrow \infty} g_n(x, y, t).$$

Using the residue theorem, we have

$$\left(\int_{-R_n}^{R_n} + \int_{C_n} \right) f(\omega) d\omega = 2\pi i \sum_k \text{Res}(f, z_k).$$

Here, C_n is a positively orientated curve that connects R_n to $-R_n$ in the complex ω -plane, such that we have a positively oriented simple closed curve, in which, we consider the residues running over k .

Thus, we may express g_n using the residue theorem as

$$g_n(x, y, t) = i \sum_k \text{Res}(f, z_k) - \frac{1}{2\pi} \int_{C_n} f(\omega) d\omega. \quad (\text{F.2})$$

Next, we want to construct a sequence R_n and curves C_n such that the second integral vanishes in the limit of n to infinity. Then, the inverse Fourier transform is given by the sum over the residues contained in the contour.

Before using the Residue theorem, it is useful to have an idea of how the function $f(\omega)$ behaves in the complex ω -plane. We first consider if it has branch cuts and secondly where the poles reside in the complex ω -plane.

Appendix F.2. Branch cuts

We first show that $f(\omega)$ does not have any branch cuts despite being defined using the square root. We show that each component of this integrand does not contain any branch cuts and then use that the composition of these non-branch cut functions also does not have any branch cuts. The non-trivial component is given by

$$\frac{\mathcal{D}(\omega)}{\tanh \mathcal{D}(\omega)} = \frac{\sqrt{i\omega}}{\tanh \sqrt{i\omega}}.$$

The branch point is given by $\omega = 0$. We use the parametrisation $z = r \exp(i\theta)/i$. A full rotation around the branch point is then found as $z = r \exp(i(\theta + 2\pi))/i$. Substituting into the above expression and using the oddness of the hyperbolic tangent function shows that the phase factors cancel and that this function does not have a branch cut in the complex plane.

The other functions of the integrand $f(\omega)$ do not have any branch cuts as well. Thus the integrand does not contain any branch cuts since the functions from which it is build do not contain any branch cuts. This makes defining the contours for the residue theorem a lot simpler.

Appendix F.3. Poles

The complex exponential is an entire function and does not have any poles. Thus, we only need to consider $G(\mathcal{D}(\omega))$. The poles of $G(\mathcal{D}(\omega))$ occur whenever we divide by zero somewhere. We consider two cases:

- $\tanh \sqrt{i\omega} \rightarrow 0$. Multiply the top and bottom of the fraction by $\tanh \sqrt{i\omega}$ to get

$$G(\mathcal{D}(\omega)) = \frac{\tanh \sqrt{i\omega} - \sqrt{i\omega}}{\tanh \sqrt{i\omega} - \mathcal{A}i\omega \tanh \sqrt{i\omega} - \sqrt{i\omega}} \rightarrow \frac{-\sqrt{i\omega}}{-\sqrt{i\omega}} = 1,$$

for $\tanh \sqrt{i\omega} \rightarrow 0$ and $\omega \neq 0$.

For $\omega \rightarrow 0$, the fraction becomes of the form “0”/“0”. This is a removable singularity, provided we define

$$G(\mathcal{D}(0)) = \frac{1}{1 + 3\mathcal{A}}.$$

Hence, $\tanh \sqrt{i\omega} = 0$ and especially $\omega = 0$ are not poles of the function $f(\omega)$.

- $1 - \mathcal{A}i\omega - \frac{\sqrt{i\omega}}{\tanh \sqrt{i\omega}} = 0$. We need to solve the following equation for ω assuming $\mathcal{A} > 0$:

$$1 - \mathcal{A}i\omega - \frac{\sqrt{i\omega}}{\tanh \sqrt{i\omega}} = 0. \quad (\text{F.3})$$

A figure suggests that these roots are located on the positive imaginary axis of the complex ω -plane. This line can be parametrised using a positive real variable $y > 0$ (since we have excluded $\omega = 0$ already) as

$$\omega = iy.$$

The following identity holds for the hyperbolic tangent and tangent for complex z :

$$\tanh iz = i \tan z.$$

We already showed that the components of $G(\mathcal{D}(\omega))$ do not have a branch cut, so it follows that

$$\frac{\sqrt{i\omega}}{\tanh \sqrt{i\omega}} = \frac{\sqrt{y}}{\tan \sqrt{y}}.$$

Equation (F.3) can therefore be expressed as the following transcendental equation for $y > 0$:

$$\tan \sqrt{y} = \frac{\sqrt{y}}{1 + \mathcal{A}y}.$$

Solving this equation exactly is difficult. For large enough y , the right-hand side goes to zero. The zeros of the tangent are given by $(k\pi)^2$ for k in \mathbb{Z} and k large enough. This shows that there are an infinite number of solutions. Let us denote them by y_k for $k = 1, 2, 3, 4, \dots$. These solutions can be determined numerically. For analytical purposes, these solution can also be approximated analytically. We use the first two iterates of Picard's method. We approximate the solution using the following estimates for $k = 1, 2, 3, \dots$:

$$\hat{y}_k = \left(k\pi + \arctan \left(\frac{k\pi}{1 + \mathcal{A}(k\pi)^2} \right) \right)^2.$$

It can be shown that these approximations of the zeros of the denominator do not coincide with the zeros of the numerator of $G(\mathcal{D}(\omega))$ for $\mathcal{A} > 0$. Hence, these are genuine poles of $G(\mathcal{D}(\omega))$

Transforming back to the ω domain, shows that the poles of $f(\omega)$ are given by

$$z_k = iy_k,$$

with $y_k > 0$ for all $k = 1, 2, 3, \dots$. And similarly for the approximate solution

$$\hat{z}_k = i\hat{y}_k. \tag{F.4}$$

Appendix F.4. Contours

The previous section has shown that the function $f(\omega)$ has an infinite number of poles along the positive imaginary axis in the ω -plane for $\mathcal{A} > 0$. The distance between two consecutive poles gets larger and larger as we move away from the origin. We want to define the contour C_n as a semicircle connecting R_n to $-R_n$ in the upper or lower half plane. We define R_n such that it stays away from the poles of $f(\omega)$. We define the radii R_n as the moduli of ω that satisfy the equation

$$\frac{1}{\tanh \sqrt{i\omega}} = 0.$$

This equation is an approximation of the true roots of $f(\omega)$.

We find the radii

$$R_n = \left(\frac{2n+1}{2} \pi \right)^2,$$

for $n = 0, 1, 2, 3, \dots$. In general, these radii do not coincide with the radii of the poles $|z_k| = |y_k|$ for $\mathcal{A} > 0$ as desired. Even if they did, we asymptotically have for large enough k :

$$|y_k| \sim (k\pi)^2,$$

such that $R_n \neq |y_k|$ for n and k sufficiently large.

Appendix F.5. Jordan's lemma

Jordan lemma states that for a function of the form

$$f(\omega) = G(\mathcal{D}(\omega)) \exp(i\omega t),$$

for $t > 0$, defined on the semicircle C_n in the upper half plane,

$$C_n = \{R_n \exp(i\theta) \mid 0 \leq \theta \leq \pi\},$$

the contour integral can be bounded by

$$\left| \int_{C_n} f(\omega) d\omega \right| \leq \frac{\pi}{t} M_n,$$

where we have defined

$$M_n = \max_{0 \leq \theta \leq \pi} |G[\mathcal{D}(R_n \exp i\theta)]|.$$

For $t < 0$, a similar result can be derived for a semicircular contour in the lower half plane C_n^* using a change of variables.

We derive a bound on the whole circle of radius R_n in the complex plane and apply this bound twice, once for negative t and once for positive t . We have

$$\begin{aligned} N_n &= \max_{0 \leq \theta \leq 2\pi} |G[\mathcal{D}(R_n \exp i\theta)]|, \\ &= \max_{0 \leq \theta \leq 2\pi} \left| \frac{1 - \frac{\sqrt{iR_n \exp i\theta}}{\tanh \sqrt{iR_n \exp i\theta}}}{1 - \mathcal{A}iR_n \exp i\theta - \frac{\sqrt{iR_n \exp i\theta}}{\tanh \sqrt{iR_n \exp i\theta}}} \right|, \\ &\leq \frac{\sqrt{R_n} + 1}{|\mathcal{A}R_n - 1|}. \end{aligned}$$

Thus in the limit of n to infinity, R_n goes to infinity and $N_n \rightarrow 0$ for $\mathcal{A} > 0$. Another method to see this is by considering the dominant terms in N_n for n to infinity. Since N_n considers a larger range of θ values than M_n , it follows that $M_n \leq N_n$ for all n . In the limit of n to infinity, we have $M_n \rightarrow 0$. Thus using Jordan's lemma for the upper half plane ($t > 0$) and lower half plane ($t < 0$), we have

$$\lim_{n \rightarrow \infty} \left| \int_{C_n} f(\omega) d\omega \right| \leq \lim_{n \rightarrow \infty} \frac{\pi}{t} M_n \rightarrow 0, \quad \text{for } t > 0, \quad (\text{F.5})$$

$$\lim_{n \rightarrow \infty} \left| \int_{C_n^*} f(\omega) d\omega \right| \leq \lim_{n \rightarrow \infty} \frac{\pi}{-t} M_n \rightarrow 0, \quad \text{for } t < 0. \quad (\text{F.6})$$

Appendix F.6. Residues

We need to determine the residues at the poles z_k . We assume that the poles are simple. We write $f(\omega)$ as a fraction as follows

$$f(\omega) = -2i \frac{p(\omega)}{q(\omega)} \exp i\omega t,$$

where we have defined

$$p(\omega) = - \left(1 - \frac{\sqrt{i\omega}}{\tanh \sqrt{i\omega}} \right), \quad q(\omega) = 2i \left(1 - \mathcal{A}i\omega - \frac{\sqrt{i\omega}}{\tanh \sqrt{i\omega}} \right).$$

Computing the derivative

$$q'(\omega) = 1 + 2\mathcal{A} + \frac{1}{\sqrt{i\omega} \tanh \sqrt{i\omega}} - \frac{1}{\tanh^2 \sqrt{i\omega}}.$$

The residues may be computed as

$$\text{Res}(f, z_k) = -2i \lim_{\omega \rightarrow z_k} \frac{p(\omega)}{q'(\omega)} \exp i\omega t.$$

We define the function

$$\eta_k(t) = i \text{Res}(f, z_k) = 2 \lim_{\omega \rightarrow z_k} \frac{p(\omega)}{q'(\omega)} \exp i\omega t. \quad (\text{F.7})$$

We derive an approximation of $\eta_k(t)$ called $\hat{\eta}_k(t)$ using the estimates of the poles given by equation (F.4). The ‘fractional’ part becomes

$$a_k = \lim_{\omega \rightarrow \hat{z}_k} \frac{p(\omega)}{q'(\omega)} = \frac{\mathcal{A}(k\pi)^4 + (\mathcal{A}(k\pi)^3 + k\pi) \arctan\left(\frac{k\pi}{1 + \mathcal{A}(k\pi)^2}\right)}{\mathcal{A}^2(k\pi)^4 + (1 + 4\mathcal{A})(k\pi)^2 - \frac{\mathcal{A}(k\pi)^2 + 1}{1 + \frac{1}{k\pi} \arctan\left(\frac{k\pi}{1 + \mathcal{A}(k\pi)^2}\right)} + 1}.$$

The approximation becomes

$$\hat{\eta}_k(t) = 2a_k \exp(-\hat{y}_k t). \quad (\text{F.8})$$

Appendix F.7. Residue theorem

We can now use the residue theorem. We consider the cases $t < 0$ and $t > 0$, separately, and then combine them.

We consider $t < 0$. From equation (F.2) and Jordan’s lemma (F.6) in the limit $n \rightarrow \infty$, we find that

$$g(x, y, t) = i \sum_k \text{Res}(f, z_k), \quad \text{for } t < 0.$$

Here, the sum of the residues runs over all residues in the lower half plane. In Appendix F.3, we did not find any poles in the lower half plane. Hence we find for $t < 0$:

$$g(x, y, t) = 0, \quad \text{for } t < 0.$$

This means that the kernel is causal, i.e., it does not depend on information from the future.

We consider $t > 0$. From equation (F.2) and Jordan’s lemma (F.5) in the limit $n \rightarrow \infty$, we have

$$g(x, y, t) = i \sum_{k=1}^{\infty} \text{Res}(f, z_k), \quad \text{for } t > 0. \quad (\text{F.9})$$

Here, the sum of the residues runs over all residues in the upper half plane, which we have conveniently numbered z_k for $k = 1, 2, \dots$

The two cases can be combined using a Heaviside step function defined as

$$H(t) = \begin{cases} 1, & t > 0 \\ 0, & t < 0. \end{cases}$$

Thus we have the following exact representation of g for general values of t and $\mathcal{A} > 0$:

$$\begin{aligned} g(x, y, t) &= H(t) \sum_{k=1}^{\infty} i \operatorname{Res}(f, z_k), \\ &= H(t) \sum_{k=1}^{\infty} \eta_k(t). \end{aligned} \quad (\text{F.10})$$

Here, we have used equation (F.7). This equation can also be approximated yielding

$$\hat{g}(x, y, t) = H(t) \sum_{k=1}^{\infty} \hat{\eta}_k(t).$$

Here, we have used equation (F.8).

Appendix F.7.1. Plots of the history kernels

We define the nondimensional time scale $t^* = \sigma t$ and the ratio $\gamma = f/\sigma$. From equation (F.1), we have the nondimensional friction kernels

$$h_1^*(t^*) = \frac{h_1(t^*)}{\sigma} = g(t^*) \cos(\gamma t^*), \quad h_2^*(t^*) = \frac{h_2(t^*)}{\sigma} = g(t^*) \sin(\gamma t^*). \quad (\text{F.11})$$

In Fig. F.8, the log of the absolute value of the nondimensionalized first history kernel h_1^* is shown as function of \mathcal{A} and the nondimensionalized time t^* for $\gamma = 0$, i.e., no Coriolis force $f = 0$. It can be seen that for very small values of the nondimensional time t^* the function attains very large values whereas if the nondimensional time t^* becomes $\mathcal{O}(1)$, the function quickly decays. Increasing the parameter \mathcal{A} past 10^{-2} seems to lead to a decrease in the history function in the plotted domain.

In Fig. F.9, the nondimensionalised history kernels h_1^* and h_2^* are plotted as functions of γ and the nondimensionalized time t^* for $\mathcal{A} = 10^{-2}$. For $\gamma = 0$, the no Coriolis case is recovered at $\mathcal{A} = 10^{-2}$. Here, a linear time axis is chosen to show the oscillatory nature of the history functions. The behaviour near $t^* = 0$ is similar to the no Coriolis case, see Fig. F.8. When

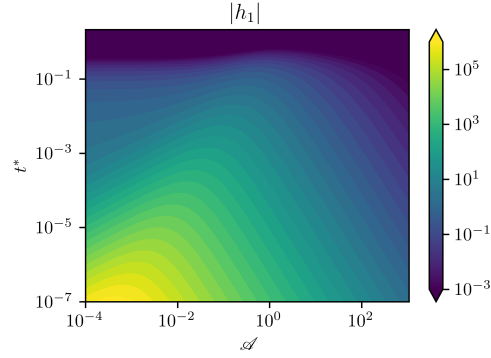


Figure F.8: The logarithm of the absolute value of h_1^* as function of \mathcal{A} and the nondimensionalized time t^* for $\gamma = 0$ including the first 20.000 components.

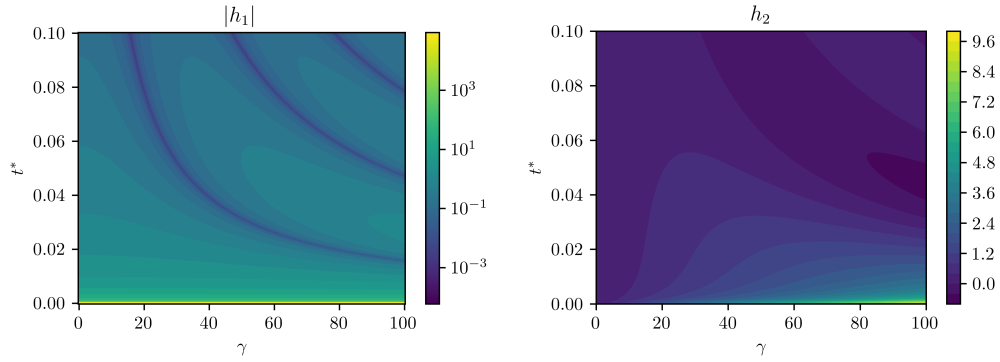


Figure F.9: The history convolution kernels as function of γ and the nondimensionalized time t^* for $\mathcal{A} = 10^{-2}$ using the first 500 components. The left figure plots the log scale of the absolute value of h_1^* , whereas the right figure shows h_2^* .

the nondimensional number γ increases, the first history function shows increasing oscillatory behaviour by the increasing number of dark blue lines. The second history function changes from zero to non-zero with the largest value attained for large values of γ and small values of t^* .

Appendix G. The equivalent 2DH equations for harmonic models

In this section, we consider the friction formulation for models that resolve multiple harmonic components, here referred to as harmonic models.

We assume that the forcing consists of N harmonic components

$$\omega^1, \omega^2, \dots, \omega^{N-1}, \omega^N.$$

Then we can expand the physical variables in the same harmonic components as the forcing since the equations are linear

$$\begin{bmatrix} \zeta \\ \bar{u} \\ \bar{v} \\ u_b \\ v_b \end{bmatrix} (x, y, t) = \sum_{n=1}^N \Re \left\{ \begin{bmatrix} Z^n \\ \bar{U}^n \\ \bar{V}^n \\ U_b^n \\ V_b^n \end{bmatrix} (x, y) \exp(i\omega^n t) \right\}.$$

Thus, we denote the dependence on the parameter ω^n using the superscript n rather than with ‘ ω^n ’ as we did before.

The derivation is very similar to the single harmonic component case. The main difference is that after substituting the above expansion into the 2DH equations and applying the appropriate averaging operator a set of equations is obtained for each frequency component ω^n (rather than a single set of equations for ω):

$$\begin{cases} i\omega^n Z^n + (D\bar{U}^n)_x + (D\bar{V}^n)_y = 0, \\ i\omega^n \bar{U}^n - f\bar{V}^n = -gZ_x^n - \frac{1}{D}s_f U_b^n, \\ i\omega^n \bar{V}^n + f\bar{U}^n = -gZ_y^n - \frac{1}{D}s_f U_b^n. \end{cases}$$

In case the forcing frequencies form a harmonic series, i.e., $\omega_n = n\omega_0$, averaging over the period $T = 2\pi/\omega_0$ suffices:

$$\mathcal{A}_m\{\cdot\} = \frac{1}{T} \int_{-T/2}^{T/2} [\cdot] e^{-im\omega_0 t} dt.$$

For general harmonic forcing frequencies where the above condition does not hold, the limit of time average may be used:

$$\mathcal{A}_m\{\cdot\} = \lim_{T \rightarrow \infty} \frac{1}{T} \int_{-T/2}^{T/2} [\cdot] e^{-i\omega_m t} dt.$$

The bed shear stress relation derived in Appendix A is valid for each each frequency component ω^n individually. Thus from equation (A.2), we find

$$s_f \mathbf{U}_b^n(x, y) = \mathbf{R}^{3D}(x, y; \omega^n) \bar{\mathbf{U}}^n(x, y),$$

with the complex-valued 2DH friction matrix given by

$$\mathbf{R}^{3D}(x, y; \omega^n) = s_f \begin{bmatrix} r_1^n \exp i\varphi_1^n & -r_2^n \exp i\varphi_2^n \\ r_2^n \exp i\varphi_2^n & r_1^n \exp i\varphi_1^n \end{bmatrix}.$$

Here, we have defined $r_{1,2}^n$ and $\varphi_{1,2}^n$ as in equation (A.6), but with ω replaced by ω^n .

For each frequency component, the equations are transformed back to the time domain to interpret the result. For each frequency component n , we have

$$\begin{cases} \zeta_t^n + (D\bar{u}^n)_x + (D\bar{v}^n)_y = 0, \\ \bar{u}_t^n - f\bar{v}^n = -g\zeta_x^n - \frac{1}{D} [r_1^n \bar{u}^n(t + t_1^n) - r_2^n \bar{v}^n(t + t_2^n)], \\ \bar{v}_t^n + f\bar{u}^n = -g\zeta_y^n - \frac{1}{D} [r_1^n \bar{v}^n(t + t_1^n) + r_2^n \bar{u}^n(t + t_2^n)], \end{cases}$$

with the time shift t_i^n for $i = 1, 2$ given by

$$t_i^n(x, y) = \frac{\varphi_i^n}{\omega^n}.$$

The boundary conditions of the depth-averaged model are the same as before, see equations (9) and (10), except that they apply for each frequency component individually.

Thus within a depth-averaged model, we see that for each frequency component n , the 3D friction formulation prescribes a friction value that is scaled and time shifted based on the frequency.